JCI insight

# CoREST complex inhibition alters RNA splicing to promote neoantigen expression and enhance tumor immunity

Robert J. Fisher, Kihyun Park, Kwangwoon Lee, Katarina Pinjusic, Allison Vanasse, Christina S. Ennis, Parisa Farokh, Scott B. Ficarro, Jarrod A. Marto, Hanjie Jiang, Eunju Nam, Stephanie Stransky, Joseph Duke-Cohan, Melis A. Akinci, Anupa Geethadevi, Eric Raabe, Ana Fiszbein, Shadmehr Demehri, Simone Sidoli, Chad W. Hicks, Derin B. Keskin, Catherine J. Wu, Philip A. Cole, Rhoda M. Alani

*JCI Insight.* 2025. https://doi.org/10.1172/jci.insight.190287.

Research In-Press Preview Dermatology Oncology Therapeutics

## Graphical abstract

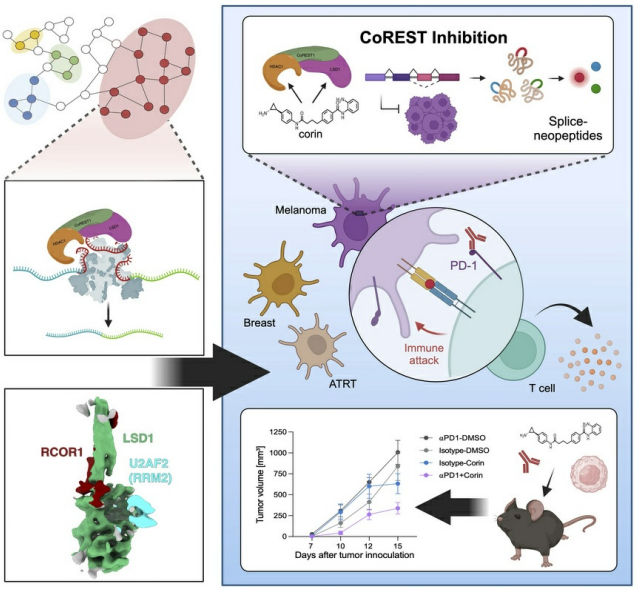


## Find the latest version:

https://jci.me/190287/pdf

# CoREST Complex Inhibition Alters RNA Splicing to Promote Neoantigen Expression and Enhance Tumor Immunity

Robert J. Fisher[1,†], Kihyun Park[1,†], Kwangwoon Lee[2], Katarina Pinjusic[3], Allison Vanasse[3], Christina S. Ennis[4], Parisa Farokh[5,6],Scott B. Ficcaro[7], Jarrod A. Marto[7], Hanjie Jiang[2], Eunju Nam[2], Stephanie Stransky[8], Joseph Duke-Cohan[3], Melis A. Akinci[3], Anupa Geethadevi[9], Eric Raabe[9], Ana Fiszbein[10], Shadmehr Demehri[5,6], Simone Sidoli[8], Chad W. Hicks[11], Derin B. Keskin[3,12], Catherine J. Wu[3], Philip A. Cole[2], Rhoda M. Alani[1*]

[1]Department of Dermatology, Boston University Chobanian and Avedisian School of Medicine; Boston, Massachusetts, USA.

[2]Division of Genetics, Departments of Medicine and Biological Chemistry and Molecular Pharmacology, Harvard Medical School and Brigham and Women's Hospital; Boston, Massachusetts, USA.

[3]Department of Medical Oncology, Dana-Farber Cancer Institute, Boston, Massachusetts, USA; Harvard Medical School; Boston, Massachusetts, USA.

[4]Cancer Center, Boston University Chobanian and Avedisian School of Medicine, Boston, Massachusetts, USA.

[5]Center for Cancer Immunology, Krantz Family Center for Cancer Research, Massachusetts General Hospital and Harvard Medical School, Boston, Massachusetts, USA.

[6]Cutaneous Biology Research Center, Department of Dermatology, Massachusetts General Hospital and Harvard Medical School, Boston, Massachusetts, USA.

[7]Department of Cancer Biology, Center for Emergent Drug Targets, and Blais Proteomics Center, Dana-Farber Cancer Institute, Boston, MA, USA; Department of Pathology, Brigham and Women's Hospital and Harvard Medical School

[8]Department of Biochemistry, Albert Einstein College of Medicine; The Bronx, NY, USA.

[9]Division of Pediatric Oncology, Johns Hopkins University School of Medicine and Johns Hopkins Hospital, Bloomberg Children's Center; Baltimore, Maryland, USA.

[10]Department of Biology, Boston University; Boston, Massachusetts, USA.

[11]Department of Pharmacology, Physiology & Biophysics, Boston University Chobanian and Avedisian School of Medicine; Boston, Massachusetts, USA.

[12]Broad Institute of MIT and Harvard, Cambridge, Massachusetts, USA; Translational Immunogenomics Laboratory, Dana-Farber Cancer Institute, Boston, Massachusetts, USA; Department of Computer Science, Metropolitan College, Boston University, Boston, Massachusetts, USA; Section for Bioinformatics, Department of Health Technology, Technical University of Denmark, Lyngby, Denmark.

*To whom correspondence should be addressed:

Rhoda M. Alani

Department of Dermatology

Boston University Chobanian and Avedisian School of Medicine

609 Albany Street

Boston, Massachusetts, 02118

Email: alani@bu.edu

Phone: 617-358-9700

**ABSTRACT** Epigenetic macromolecular enzyme complexes tightly regulate gene expression at the chromatin level and have recently been found to colocalize with RNA splicing machinery during active transcription; however, the precise functional consequences of these interactions are uncertain. Here, we identify unique interactions of the CoREST repressor complex (LSD1-HDAC1-CoREST) with components of the RNA splicing machinery and their functional consequences in tumorigenesis. Using mass spectrometry, in vivo binding assays, and cryo-EM we find that CoREST complex-splicing factor interactions are direct and perturbed by the CoREST complex selective inhibitor, corin, leading to extensive changes in RNA splicing in melanoma and other malignancies. Moreover, these corin-induced splicing changes are shown to promote global effects on oncogenic and survival-associated splice variants leading to a tumor-suppressive phenotype. Using machine learning models, MHC IP-MS, and ELISpot assays we identify thousands of neopeptides derived from unannotated splice sites which generate corin-induced splice-neoantigens that are demonstrated to be immunogenic in vitro. Corin is further shown to reactivate the response to immune checkpoint blockade, effectively sensitizing tumors to anti-PD1 immunotherapy. These data position CoREST complex inhibition as a unique therapeutic opportunity which perturbs oncogenic splicing programs while also creating tumor-associated neoantigens that enhance the immunogenicity of current therapeutics.

**Keywords: CoREST, Melanoma, RNA splicing, Cryo-EM, Immunotherapy, Neoantigens**

**Main Text:**

## INTRODUCTION

Pre-mRNA splicing is essential for the expression of >95% of human genes which encode a diverse array of highly lineage and context-dependent protein variants (1,2). Splicing changes are commonly seen in cancer, where tumors have been noted to have up to 30% more alternative splicing events (ASEs) than corresponding normal tissues, suggesting particular growth advantages of such changes (3,4). The prevalence and impact of tumor-associated splicing changes have been recognized as a critical hallmark of cancer (5–7) and splicing mechanisms have been implicated in resistance to cancer therapies (8,9). Additionally, alternative RNA splicing increases proteomic diversity in tumors and induces expression of potential neoantigens for tumor-specific detection. These splice-neopeptides have been leveraged as immunotherapy targets (3,10–12) and shown to elicit antigen-specific T cell activity to trigger an anti-tumor response (13,14); therefore, chemical induction of RNA splice modifications (15,16) and therapies targeting pre-mRNA splicing in cancer are of great interest (11,15,17).

Epigenetic macromolecular enzyme complexes tightly control gene expression at the chromatin level and have been shown to regulate transcript diversity through direct regulation of RNA splicing (18–25). RNA splicing occurs largely cotranscriptionally, and alternative splice site choice is influenced by RNA polymerase II (Pol II) elongation rate, chromatin remodelers, and histone deacetylases (2,22,26); however, the precise role of epigenetic complexes in RNA splicing is uncertain. During active transcription, histone modifying enzymes, nucleosome remodelers, general transcription factors, and the splicing machinery all localize within the same chromatin environment allowing for co-transcriptional crosstalk (20). Epigenetic proteins have been found to modulate splicing by altering splicing factor gene expression (27,28) and function (29), interacting with spliceosomal and ribonucleoprotein complexes (30), regulating the acetylation states of

splicing-associated histone marks and splicing factors (30), and altering novel splice junctions with transposable elements (31).

The CoREST epigenetic repressor complex has core subunits HDAC1 (or close paralog HDAC2), LSD1 demethylase, and the scaffold protein CoREST and was originally identified as a corepressor complex for the transcription factor REST (32). CoREST functions as a gene silencing complex through its histone deacetylase roles and demethylation of H3K4me (33,34) and has been demonstrated to deacetylate the C-terminal domain (CTD) of the catalytic subunit of RNA Pol II as part of its transcriptional repressing effects (35). We have previously described the dual LSD1/HDAC1 CoREST-selective inhibitor, corin (36), and demonstrated its antineoplastic activity in melanoma (36,37), diffuse glioma (38), malignant peripheral nerve sheath tumor (39), and colon cancer (40). Here, we explore the role of the CoREST complex in RNA splicing regulation in melanoma. We uncover interactions between the CoREST complex and splicing factors, characterize these interactions using cryogenic electron-microscopy (cryo-EM) and define a noncanonical role for CoREST in RNA splicing regulation. We find that corin widely disrupts the CoREST complex-mediated splicing program in melanoma leading to induction of immunogenic neoantigen expression in cell lines. We further demonstrate that CoREST complex inhibition significantly reactivates the response to checkpoint blockade immunotherapy in immune cold tumors. We therefore suggest that CoREST complex inhibition represents a unique therapeutic opportunity in cancer.

## RESULTS

### The CoREST complex interacts with RNA splicing factors

The CoREST complex influences gene expression and is recruited to target genes through interactions with lineage-specific transcription factors, core transcription complex components and chromatin-associated proteins (33,41) and has been shown by us and others to promote tumor growth in melanoma and other cancers (36–40). In order to further define the mechanism of CoREST complex effects in melanoma, we evaluated its protein interactions in the setting of the CoREST inhibitor, corin (2.5 μM, 24h), versus DMSO control in two melanoma cell lines (1205Lu and 451Lu) (**Figure 1A-D; Supplementary Table 1 and 2**). The LSD1/RCOR1 endogenous protein interactome was evaluated by liquid chromatography with tandem mass spectrometry (LC–MS/MS). LSD1 and RCOR1 were found to interact with all known CoREST complex subunits as well as the chromatin structural organizer, CTCF(24), and several members of the SWI/SNF (BAF) complex, as has been previously described (42). Interestingly, the CoREST complex-BAF interactions were disrupted by corin in both cell lines (**Supplementary Table 2**). Pathway analysis of proteins that showed elevated binding to LSD1 and RCOR1 over background across both cell lines identified significant enrichment for RNA splicing-related pathways, suggesting CoREST complex-splicing factor interactions in melanoma that are disrupted by corin (**Figure 1B**).

To identify high-confidence CoREST complex-interacting splicing factors (SFs), we overlapped SFs found in both LSD1 and RCOR1 pulldowns (**Figure 1C**) then stratified the data by proteins that gain or lose interaction with the CoREST complex upon corin treatment (**Figure 1D and Supplementary Table 2**). We identified 15 SFs that interacted with the CoREST complex (**Figure 1C**) and found that corin disrupts 14 out of the 15 CoREST complex-SF interactions (**Figure 1D**). To validate these findings, we selected two candidate SFs, U2 small nuclear RNA auxiliary factor 2 (U2AF2) and Serine/Arginine Splicing Factor 1 (SRSF1) based on the list of 15 CoREST complex-interacting SFs cross-referenced with an HDAC1 IP-MS dataset and their

known functions in cancer (43,44), and performed IP-WB in an additional melanoma cell line (SKMEL5) (**Figure 1E**). The CoREST complex was found to interact with both U2AF2 and SRSF1 by IP-WB and corin treatment greatly reduced CoREST-U2AF2 interactions (**Figure 1E**). To determine whether the interaction between CoREST and U2AF2 is direct, we performed a GST pull-down assay using purified proteins (**Figure 1F and G**). Full-length LSD1 protein was purified from a bacterial expression system, whereas the recombinant CoREST complex (LHC), which included LSD1, HDAC1, and RCOR1 (amino acids 86-485) proteins, was obtained from overexpression in human 293F cells, and GST-tagged U2AF2 (amino acids 83-482) and SRSF1 proteins were generated from bacterial expression (**Figure 1F**). GST pull-down assays show that both LHC and LSD1 bind to U2AF2 and SRSF1 revealing direct interactions of LHC with U2AF2 and SRSF1, with LSD1 playing a key role in this interaction (**Figure 1G**).

**Cryo-EM structure of the CoREST complex bound to U2AF2**

In order to clarify the nature of CoREST complex interactions with the splicing machinery, we sought to develop structural details relevant to these complexes using cryo-EM analysis. Our studies were focused on the CoREST complex-U2AF2 interaction as U2AF2 displayed tighter binding with the CoREST complex in AlphaFold (45) predictions compared to SRSF1. We determined the cryo-EM structure of U2AF2 bound to LSD1 + RCOR1 **(Supplementary Figure 1A)** at a global resolution of 5.14 Å **(Supplementary Figure 1B)**.

To prepare cryo-EM samples, we purified the LSD1 (a.a. 171-852) and RCOR1 (a.a. 286-485) complex (truncated LC) and U2AF2 (a.a. 241-471) proteins separately (**Figure 1F**), mixed truncated LC with U2AF2 (a.a. 241-475) at a 1:5 ratio in the absence of crosslinker and performed size-exclusion purification to isolate the U2AF2-bound LSD1/RCOR1 complex (**Figure 2A**). The chromatogram showed a peak corresponding to the LSD1-RCOR1-U2AF2 in complex, as well as

two separate peaks for LSD1-RCOR1 and U2AF2 alone, confirming that the LSD1-RCOR1 complex binds U2AF2. Fractions containing the LSD1-RCOR1-U2AF2 complex were pooled (22-25) and samples were frozen onto cryo-EM grids. Of note, the U2AF2 (a.a. 241-475) construct used for the cryo-EM sample contains two structured globular domains, the RNA Recognition Motif 2 (RRM2) and U2AF2 Homology Motif (UHM) **(Figure 2B)**.

We observed well-resolved EM density for the LSD1+RCOR1 complex, low-resolution density for U2AF2 adjacent to the side of LSD1, and some unassigned very low-resolution density in contact with the opposite side of LSD1 **(Figure 2C)**. The resolution of the EM density corresponding to LSD1+RCOR1, at ~5.0 – 6.0 Å **(Supplementary Figure 1C)**, was sufficient to unambiguously rigid fit the crystal structure of the LSD1+RCOR1 complex (PDB: 2IW5)(46) within the EM map **(Supplementary Figure 1D)**. Therefore, our cryo-EM structure, the first cryo-EM structure, to our knowledge, of the LSD1+RCOR1 complex, appears to adopt a similar conformation to the crystallized form of the LSD1+RCOR1 complex (46,47).

The resolution of the adjacent U2AF2 EM density, at 6.0 – 7.0 Å, was found to be lower than the LSD1+RCOR1 complex **(Supplementary Figure 1C)**. We therefore compared the relative size of the two U2AF2 globular domains within the EM map **(Supplementary Figure 1E and F)** and determined that the adjacent U2AF2 density is likely to be the RRM2 domain of U2AF2, as opposed to the UHM domain. The resolution for the RRM2 EM density was not high enough to determine an accurate orientation of the model within the EM map, likely due to its extensive conformational heterogeneity; however, we were able to determine that the structured RRM2 domain does not directly contact LSD1 **(Figure 2C and D)**. The additional EM density contacting LSD1 opposite the RRM2 domain could not be assigned **(Figure 2C**), although it is possible that the unassigned density may represent the UHM domain of U2AF2.

To better understand the mechanism of RNA recognition by U2AF2 in the context of the LSD1+RCOR1+U2AF2 complex, we performed an AlphaFold3 (45) multimer calculation of LSD1+RCOR1+U2AF2+RNA. As an input, we provided the same sequences as the constructs of the LSD1, RCOR1, and U2AF2 employed in the cryo-EM analysis plus added an additional 11 base-pairs of RNA **(see Methods)**. The AlphaFold prediction revealed a structured LSD1+RCOR1 at very-high confidence and showed the RRM2 and UHM domains of U2AF2 bound to LSD1 at moderately high confidence **(Figure 2E and F)**. The predicted local distance difference test (pLDDT), representing local structural confidence calculated by AlphaFold, shows that the two globular domains of U2AF2 (RRM2 and UHM) have high confidence scores, while the flexible linker loop connecting them has low scores (**Figure 2F**) demonstrating AlphaFold prediction of U2AF2 remaining folded in globular domains and associated with LSD1+RCOR1 as observed in the cryo-EM structure. Superimposing the AlphaFold structure of the RRM2 domain of U2AF2 over our cryo-EM structure shows the AlphaFold model of RRM2 in close proximity to the cryo-EM model of RRM2 **(Figure 2G)**. The AlphaFold prediction also revealed RNA bound to the RRM2 domain of U2AF2 **(Figure 2E)**, a binding mode that has been previously observed in crystal structures of RNA bound to U2AF2 (48,49). While we did not include RNA in our cryo-EM sample, the position of the RRM2 domain of U2AF2 could also accommodate bound RNA. To characterize the RRM2-UHM domains of U2AF2 in the interaction with LSD1/RCOR1, microscale thermophoresis (MST) was performed. The His-tag U2AF2 fragments (amino acids 85–471 or 241–471) were labeled with a Cy5 dye at lysine residues (Fluor-U2AF2) using a reactive NHS-ester dye. The labeling was verified using a capillary scan on the MST instrument **(Supplementary Figure 1G and H)**. Subsequently, the labeled U2AF2 fragments were mixed with serially diluted truncated LSD1/RCOR1, and MST traces were measured to calculate the dissociation constant ($K_D$) values **(Supplementary Figure 1I and J)**. We found that U2AF2 241–471, composed of RRM2 and UHM, exhibited a $K_D$ value of 16 μM comparable to that of U2AF2 85–471 ($K_D$ 14 μM), indicating that U2AF2 directly binds to truncated LSD1/RCOR1 with a

moderate binding affinity, and that the RRM2 and UHM domains of U2AF2 are critical for this interaction. Additionally, a GST pull-down assay using the RRM2 fragment of U2AF2 confirmed that the RRM2-only fragment binds to truncated LSD1/RCOR1 **(Supplementary Figure 1H)**, consistent with Cryo-EM and AlphaFold data, further supporting the role of the U2AF2 RRM2 domain in binding to CoREST.

**CoREST complex regulation of splicing factor gene expression**

Given our findings of the CoREST complex binding to components of the RNA splicing machinery which is diminished in the context of the CoREST inhibitor, corin, and the fact that expression of RNA binding proteins (RBPs) is widely dysregulated in solid tumors (50), we sought to determine whether the CoREST complex may directly impact the transcription of pre-mRNA splicing factors. We conducted RNA-sequencing on six melanoma cell lines treated with corin (2.5μM, 24h), three tumor cell lines designated as $MITF^{high}/AXL^{high}$ cell lines (differentiated phenotype) (51) and three tumor cell lines designated as $MITF^{low}/AXL^{high}$ (dedifferentiated phenotype) (51). We then performed gene set enrichment analysis (GSEA) to identify commonly enriched pathways following corin treatment across all cell lines regardless of phenotypic status. Remarkably, we identified the KEGG Spliceosome pathway as the most common downregulated pathway across all six cell lines (**Figure 3A and B**) suggesting that CoREST inhibition downregulates splicing factor gene expression in melanoma regardless of molecular phenotype. Further analysis of the splicing factor genes impacted by corin treatment revealed that, although many U2-related and early spliceosomal genes were downregulated, a broad range of spliceosome and trans-acting splicing regulators were also downregulated suggesting widespread impact on the splicing machinery (**Figure 3C and Supplementary Figure 2A**). Notably, 29% of genes in the KEGG Spliceosome gene set were found to be consistently downregulated by corin without correlation to melanoma phenotype, highlighting the broad impact of CoREST on splicing factor gene regulation. To validate these findings, western blotting was performed on the three most

downregulated genes, where U2AF2 and ALYREF were both noted to be significantly decreased in expression at the protein level following corin treatment (**Figure 3D, E, and Supplementary Figure 2B**). This is particularly of interest since melanoma (TCGA SKCM) patients with decreased U2AF2 expression have significantly prolonged survival (p=0.001; **Figure 3F**).

To determine whether corin-associated decreases in splicing factor expression were due to direct transcriptional changes, we performed PRO-seq on SKMEL5 cells treated with corin and used the 3' nascent RNA reads to conduct differential gene expression analysis (**Supplementary Fig. 2C**). We found the KEGG Spliceosome pathway to be significantly negatively enriched in the setting of corin treatment with over 50% of splicing factor genes downregulated in the RNA-seq also downregulated in the PRO-seq (**Supplementary Figure 2D**). This suggests that corin-associated splicing factor downregulation is due to direct effects on mRNA synthesis rather than transcript stability. As CoREST is an epigenetic repressor complex and the majority of corin effects on tumor cells are associated with transcriptional upregulation (36–39), it is anticipated that these transcriptional repressive effects of corin on splicing factor genes are principally associated with indirect transcriptional changes. Since we were able to demonstrate decreased transcription of SF genes in the setting of corin in melanoma cells, we sought to determine whether the loss of CoREST complex-SF protein interactions in the setting of corin was due to decreased expression of splicing factor proteins, or a disruption of CoREST complex-SF binding. Using V5-tagged U2AF2 overexpression in SKMEL5 melanoma cells, we found that binding of V5-U2AF2 to CoREST (RCOR1) was significantly inhibited in the setting of corin treatment without a change in V5-U2AF2 expression supporting a specific inhibitory effect of corin on U2AF2 binding to CoREST independent of the transcriptional effects on U2AF2 (**Figure 3G**).

**Corin induces RNA splicing changes in melanoma**

Given the observed CoREST complex-U2AF2 interactions and corin's impact on splicing factor gene expression, we next sought to determine the functional effects of corin on RNA splicing across a panel of melanoma cell lines. Two computational tools were used to analyze our RNA-seq data for changes in splicing events. rMATS (52) was applied to detect alterations in skipped exons (SE), 3' splice sites (3'SS), 5' splice sites (5'SS), and mutually exclusive exons (MXE), while AltAnalyze (53) was used to identify changes in retained introns (RI). Using these methods, we identified thousands of splicing events modified by corin treatment across the six melanoma cell lines tested (**Figure 4A, Supplementary Figure 3, and Supplementary Table 3**), with skipped exons being the most frequently affected. When we compared PSI (percent spliced in) values of SE events between DMSO and corin treatment, all cell lines except WM793 showed a significant decrease in PSI distribution in the setting of corin treatment indicating increased exon skipping with CoREST complex inhibition (**Figure 4B**). Additionally, when we compared the exon architecture of skipped versus included exons, skipped exons were significantly shorter, flanked by long introns, and in lower GC content regions of the genome (**Supplementary Figure 4A and B**). This suggests that the CoREST complex may be involved in promoting exon inclusion preferentially at defined exon architecture during co-transcriptional RNA splicing.

Next, we compared the unique SE events stratified by MITF status to determine whether the CoREST complex may be responsible for driving a phenotypic splicing program (**Figure 4C**). We identified several phenotype-specific SE events, with 63 events associated with the differentiated ($MITF^{high}$) state and 62 associated with the dedifferentiated ($MITF^{low}$) state; however, the overlap was minimal relative to the total number of SE events across the cell lines. We did, however, find 129 SE events that were commonly induced by corin treatment across all melanoma cell lines, which may be more generalizable targets of CoREST complex-specific splicing **(Figure 4D)**. Although, these common SE events comprise a small fraction of the total, gene ontology analysis of corin-induced differential exon inclusion conducted independently on each cell line

demonstrated that many of the same biological processes were impacted by corin treatment such as cell motility, cytoskeletal structure, and GTPase activity (**Figure 4E**).

Given the impact of CoREST complex inhibition on SF binding to the CoREST complex and SF transcription, we next sought to determine the effect of corin on intron-containing pre-mRNA splicing activity by comparing the PSI distribution of intron retention events identified by AltAnalyze and found no significant directional increase in retention. We further compared the pathways impacted by intron retention to those impacted by exon skipping and found that RNA splicing factors are most differentially impacted by corin-induced intronic splicing (**Supplementary Figure 4C and D**). In order to define the splicing factors that drive the CoREST complex's impact on RNA splicing, we utilized RNA-SPRINT (54) to estimate individual RNA Binding Protein (RBP) activity across all six cell lines under each treatment condition and correlated the activity scores to the expression level of the corresponding RBP using Spearman's rank correlation (**Supplementary Figure 5A**). Four candidates (SF3B4, HNRNPC, HNRNPK, and U2AF2) had significant coefficients ($\rho > 0.5$) in which decreased expression was strongly correlated with decreased RBP activity (**Supplementary Figure 5B-D**), suggesting that CoREST complex-induced splicing programs could be largely attributed to the functions of these particular splicing factors. Overall, these findings highlight the complexity of RNA splicing regulation, as we see the CoREST complex engaged in transcriptional, translational, and post-translational modifications that control the splicing process as well as specific splicing of splicing-associated transcripts.

Next, we validated 3 common SE events associated with cytoskeletal structure and cell motility functions with demonstrated oncogenic associations by RT-PCR (**Figure 4F; Supplementary Figure 6A-C**). Myosin-1b (MYO1B) is a motor protein critical for actin filament organization and is crucial for neuronal development. *MYO1B* exon 23 exclusion has been associated with

decreased cell migration and significant survival outcomes in glioblastoma mouse models (28). Fibronectin (*FN1*) exon 33 encodes extra domain A which has been shown to increase tumor metastasis and is widely expressed in melanoma tissues compared to normal skin (55). Tight Junction Protein 1 (*TJP1* or *ZO-1*) exon 20 encodes the alpha domain whose skipped isoform is increased in breast, lung, and colon cancers (56) and has been shown to enhance actin stress fiber assembly, increase cell migration, and be induced during EMT by TGFB (56). In all instances, we found that corin significantly reversed tumor-associated splice isoforms (**Figure 5A; Supplementary Figure 6A-C**); moreover, we found that corin significantly reversed CoREST complex-mediated splicing events to a greater extent than either MS-275 or GSK-LSD1 alone, or the combination of inhibitors (**Figure 5A; Supplementary Figure 6A-C**) suggesting targeted impacts of the dual-specificity CoREST complex inhibitor. Interestingly, we did not see any significant impact of U2AF2 on either LSD1 demethylase or LHC deacetylase activities in purified enzyme assays (**Supplementary Figure 7A-C**), indicating a unidirectional impact of CoREST activity on the splicing machinery.

Based on our finding that CoREST complex-U2AF2 interactions are disrupted in the setting of corin, we hypothesized that these differential exon inclusion events may be directly influenced by CoREST-SF recruitment to RNA. Using RIP-qPCR with primers flanking *FN1* exon 33 and *MYO1B* exon 23, we found that CoREST complex subunits (LSD1 and RCOR1) and SFs (U2AF2 and SRSF1) not only bind RNA at these splice sites but also significantly lose occupancy with corin treatment (**Figure 5B**), suggesting that CoREST complex-SF recruitment to alternative splice sites can directly impact exon inclusion levels.

Given the impact of corin on tumor-associated splicing events, we analyzed the 129 corin-induced common SE events in the 6 melanoma cell lines for survival-association in TCGA-SKCM (human skin cutaneous melanoma) using OncoSplicing and a cox regression model (57). Eight of the

common splicing events were found to be directionally beneficial for overall survival across TCGA SKCM patients (**Figure 5C**) including *FN1* exon 33, where exon exclusion was found to be associated with significantly improved survival outcomes (**Figure 5D**).

As mRNA synthesis rates have been shown to have a significant impact on splicing, we were curious to see if CoREST could regulate RNA splicing by influencing the rate of active transcription. A previous study found that the CoREST complex can directly bind to RNA polymerase II after the pre-initiation complex is formed to deacetylate the CTD and effectively pause the polymerase (35). We hypothesized that this noncanonical role of the CoREST complex could alter RNA synthesis kinetics, and thus alter exon inclusion levels. To test this, we analyzed our PRO-seq data for changes in Pol II coverage at alternatively included exon splice sites in the setting of corin. Although we found that inhibiting the CoREST complex led to significant promoter-proximal pause release genome-wide (**Supplementary Figure 8A, B; Supplementary Table 4**), we did not note a significant difference in Pol II coverage between included or excluded exons (**Supplementary Figure 8C**), suggesting that these alternative splicing changes occur independent of a corin-induced kinetic effect on Pol II pause release.

**Corin induces RNA splicing changes across cancers**

Given the broad impact of corin on the splicing machinery in melanoma, we were interested in determining whether corin could modulate splicing across other cancers. Comparison of the expression levels of splicing factors transcriptionally downregulated by corin treatment between normal and matched tumor samples in cBioPortal revealed that many of these factors are significantly overexpressed in a diverse array of tumors (**Figure 6A and Supplementary Figure 9**), suggesting that this may be a driver event in cancers which could potentially be targeted by corin. We next sought to determine whether corin-induced splicing changes could be seen in other cancers using a bioinformatic approach. Data obtained from two independent external RNA-

sequencing datasets using cancer cells treated with corin, an ER+ breast cancer dataset (42) and an Atypical Teratoid Rhabdoid Tumor (ATRT) dataset (58), were mined for gene expression changes and differential splicing analysis was performed using the pipeline previously described. Remarkably, we found that corin significantly impacted splicing factor gene expression within these tumor cells to a similar extent to that seen in melanoma ($p < 0.001$; **Figure 6B, C; Supplementary Table 5**) and promoted thousands of RNA splicing differences across both tumor types (**Fig. 6D, Supplementary Figure 10A, and Supplementary Table 6**). Moreover, the pathways affected by corin-induced splicing included many of the same cell motility and GTPase pathways seen in melanoma (**Figure 6E and F**) suggesting not only that corin can induce splicing changes across cancer types, but also that the CoREST complex may be involved in regulating splicing of specific biological processes in cancer. Notably, the differences in splicing events represented in **Figure 6E** are likely driven by intrinsic differences in epigenetic and transcriptional profiles rather than cell line-dependent CoREST-regulated splicing mechanisms. Concordance analysis of SE events shared between melanoma cell lines reveals strong concordance (>90%) as measured by PSI directionality (**Supplementary Figure 10A and B**). Differential alternative promoter (AP) events, which most closely reflect distinct transcriptional programs, display even higher concordance (>95%) and cluster by MITF phenotypic status (**Supplementary Figure 10C**). Despite few phenotype-specific AP events (**Supplementary Figure 10D**) and diverse cell line-specific pathways (**Supplementary Figure 10E**), this concordance suggests CoREST-regulated splicing mechanisms are conserved but depend on intrinsic epigenetic landscapes."

**Corin-induced splice-neoantigens are presented on human MHC and are immunogenic**

The splicing events discussed thus far have arisen from known annotations; however, we found that many events induced by corin were derived from unannotated splice sites and hypothesized that these unannotated events would have the potential to produce neopeptide products that may elicit an immune response in vivo (15,16). To identify neopeptide candidates, we utilized a

combination of predictive computational methods and HLA IP-mass spectrometry validation (**Figure 7A**). SpliceTools (59) and SNAF (54) were used to identify 8-11mer neopeptides produced from significant splicing events ($q < 0.05$, $|deltaPSI| \geq 0.1$, $log2TPM > 3$). Remarkably, we identified thousands of neopeptide sequences induced by corin treatment across all melanoma cell lines and found them to be induced in a cell-line dependent manner (**Figure 7B and C**) akin to the cell-line specific splicing patterns identified previously (**Figure 4**). In order to assess HLA binding of predicted neopeptides we utilized two machine learning models trained on patient mass spectrometry data: NetMHCpan4.1 (60) and HLAthena (61). We found hundreds of neopeptides predicted to bind (%Rank < 2) SKMEL5 cell HLAs by both tools (**Figure 7D**) and overlapped the neopeptides identified by each tool for each allele to identify the best candidate peptides (**Figure 7E**). Corin-associated neopeptides were then ranked based on a scoring system taking HLA binding rank, junction count, and deltaPSI value into consideration (**Figure 7F and Supplementary Table 7**). HLA-IP mass spectrometry was used to investigate the 556 predicted neopeptide targets. Remarkably, we recovered over 10,000 8-11mer peptides in each replicate of mass spec and found 7462 corin-specific peptide products (**Figure 7G and Supplementary Table 8**). When we overlapped those products with the predicted 556 candidate neopeptides, we found 2 neopeptides that were produced from corin-specific splicing (**Figure 7H**). To assess if any neopeptides were missed, we also overlapped the 7462 corin-specific peptides with the human proteome and found the 2 neopeptides already predicted. Lastly, we used the deep learning model, DeepImmuno (62), to predict the immunogenicity score of each peptide to its respective strongest binding HLA allele. Both peptides validated by mass spec were predicted to be immunogenic (immunogenicity score > 0.5) and were further tested in immunogenicity assays. Additionally, we ranked the top predicted peptides based on immunogenicity score and tested the top two unique peptides in our immunogenicity assay (**Figure 7I**). Since HLA-C alleles do not have adequate training data for accurate DeepImmuno immunogenicity predictions, we focused on HLA-A and HLA-B binding peptides.

To test the immunogenic potential of the four candidate neoantigens, we loaded high purity synthetic peptides on antigen presenting cells (APCs) derived from HLA-matched PBMCs (A11:01, B40:01, C03:04) and assessed pre-stimulated CD8+ T cell activation in an IFN-γ Enzyme-Linked ImmunoSpot (ELISpot) assay (**Figure 7J, K; Supplementary Figure 11A and B**). Two of the four neopeptides elicited strong T cell activation when loaded on A11:01 APCs compared to a DMSO negative control and CEF pool positive control confirming that corin treatment can induce splice-neoantigens in human melanoma cells that are immunogenic.

**Corin treatment sensitizes immune cold tumors to immunotherapy**

Given our finding of corin-induced expression of immunogenic neoantigens, we sought to evaluate corin treatment of melanoma in an immune competent mouse model in conjunction with immune checkpoint blockade (ICB) in an immune "cold" melanoma model. The B16-F10 melanoma mouse model was established with treatment arms including vehicle, α-PD1, corin, and the combination of α-PD1 + corin (**Figure 8A**) and tumors were measured starting 7 days after inoculation. Remarkably, the combination α-PD-1 + corin treatment was found to decrease tumor growth by 66% as measured by tumor volume and tumor weight compared to α-PD1 treatment alone within one week of initiating therapy (**Figure 8B-D**). Additionally, there were no significant changes in body **(Figure 8E**) or spleen weight (**Figure 8F**) suggesting that corin treatment is tolerated at the treatment dose. In order to assess the impact of corin treatment on the immune microenvironment, we isolated CD45+ cells from α-PD1 and α-PD1+corin tumors and evaluated them by single-cell RNA sequencing (scRNA-seq) (**Figure 8G-L; Supplementary Figure 11C-F**). 23,000 tumor-enriched CD45+ cells were profiled, analyzed by Uniform manifold approximation and projection (UMAP), and segregated into 17 clusters based on the expression of leukocyte-associated genes and enrichment of gene signatures from external single-cell datasets (**Figure 8G-J**) (63). This process allowed us to define major canonical T cell phenotypes

such as naive T cells (Tn), exhausted cells (Tex), CD8+ cytotoxic T lymphocytes (CTLs), regulatory T cells (Treg), and cycling cells (Tcyc) as well as monocyte/macrophage lineages, B cells, neutrophils, dendritic cells and plasma cells (**Supplementary Figure 11C and D**). Strikingly, T cells from the αPD-1 treated tumors were primarily Tn cells (43%) and Tex (19%) whereas T cells from the corin+ αPD-1-treated tumors underwent significant expansion of CTLs (57%) which supports induction of a CTL response by tumor-associated neoantigens (**Figure 8I, J, and Supplementary Figure 11E**). Differential gene expression analysis in the T cell populations from αPD-1 versus αPD-1+corin treated tumors showed significant upregulation of granzyme B (*Gzmb*), interferon gamma (*Ifng*) and Cd8a along with significant downregulation of transcription factor 7 (*Tcf7*), lymphoid enhancer binding factor 1 (*Lef1*), and L-selectin (*Sell*) (**Figure 8K and Supplementary Figure 11F**). Gene set enrichment analysis (GSEA) demonstrated enhanced cytokine activity, leukocyte migration inflammatory response, antigen response, and tumor-associated immune response in T cells isolated from αPD-1+corin treated tumors versus αPD-1 treatment alone (**Figure 8L**), consistent with T-cell activation in response to tumor-associated neoantigen expression while staining of tumors for CD3+ and CD8+ T cells showed increased CD8+ cells in the αPD-1+corin treated tumors versus αPD-1 treatment alone (**Supplementary Figure 11G**).

## DISCUSSION

Regulation of RNA splicing is critical across all cell types to maintain normal biological functions including cell growth and differentiation (63,64), while perturbations in splicing are widely seen in cancers (65). Here we establish a role for the CoREST complex in mediating tumorigenesis via direct interactions with the RNA splicing machinery as demonstrated by proteomic analysis, biochemical studies, and cryo-EM structural data. Further, we define a role for corin in inhibiting

these interactions and promoting alternative splicing in tumor cells. Remarkably, we find that the CoREST complex modulates pre-mRNA splicing via a variety of mechanisms including direct binding to the 3' splice site recognition factor, U2AF2, and enhanced splicing factor transcription, both of which are inhibited by corin. Importantly, we define the region of binding of LSD1/RCOR1 to U2AF2 as being within the RRM domain of U2AF2 (66,67), which interfaces with the DNA binding domain of LSD1 (47) suggesting potential competing affinities for LSD1 at this site for transcriptional versus splicing-associated regulatory functions. While we did not include RNA in our cryo-EM sample, the position of the RRM2 domain of U2AF2 could also accommodate bound RNA if it binds to RRM2 in a similar manner as depicted in the AlphaFold prediction. Additionally, we find both LSD1 and RCOR1 as well as splicing factors U2AF2 and SRSF1 to be located at critical splice junctions of tumor-associated splice variants and that these interactions are all inhibited in the setting of corin, further supporting functional interactions of splicing factors and the CoREST complex in cancers; conversely, U2AF2 does not significantly impact LSD1 demethylase activity or LHC deacetylase activity.

Our evaluation of CoREST complex effects on pre-mRNA splicing activity allowed us to identify significant corin-induced alternative splicing events across melanomas regardless of tumor subtype, with the greatest influence on skipped exon and retained intron activities. Although such effects of chromatin remodeling enzymes, and HDACs in particular, have been identified in the past and largely been attributable to kinetic coupling of transcription to splicing changes (30), our PRO-seq analysis of corin-treated cells revealed that there were no changes in Pol II kinetics. This suggests that corin-induced alternative splicing events are the result of direct effects on splicing factor transcription and interactions of the CoREST complex with the splicing machinery, rather than splicing alterations related to Pol II rate changes. Remarkably, we find that corin-induced splicing changes are not unique to melanoma, as common significant pathways are also seen in ATRT and breast cancers, as identified through bioinformatic analyses, suggesting that

corin-induced splicing differences may be more generally applicable to a large number of cancers. Additionally, we demonstrate that splicing events induced by corin lead to the expression of neopeptides that elicit an immune response *in vitro*, while corin treatment of melanoma in an immune competent mouse model leads to significant inhibition of tumor growth in conjunction with immune checkpoint blockade (ICB), rendering an immune-cold melanoma sensitive to checkpoint inhibition. Collectively, these data suggest the potential significant and broad application of corin to enhance immune-mediated responses to cancers.

While previous investigations have demonstrated the utility of pharmacologic induction of RNA splicing to promote neoantigen expression and anti-tumor immunity in preclinical studies (15,16), and several drugs targeting the splicing machinery have been evaluated in clinical trials (5,68), the vast majority of these reagents have not progressed in clinical development due to limited efficacy as single agents (5,69,70). Our identification of a role for the CoREST complex in binding to splicing factors and the use of the small molecule CoREST inhibitor, corin, to promote alternative splicing events in cancer leading to neoantigen expression and T cell-mediated immunity represents a potential approach to promote immunoreactive neoantigen expression in immune-cold tumors. Indeed, studies suggest a link between tumor mutational burden (TMB), the presence of neoantigens on MHC molecules and responses to ICB therapy in cancers (71–74). We were therefore interested to see that corin induced thousands of alternative splicing events in both a high-TMB tumor (melanoma) as well as a low-TMB tumor (ATRT) suggesting that corin treatment of ATRT may also result in significant neoantigen expression and induced tumor immunity. We also note that corin induced alternative splicing events at critical splice junctions to a greater extent than either HDACi (MS-275) or LSDi (GSKLSD1) alone or in combination suggesting improved efficacy of corin versus either agent not only on tumor growth[36], but also within the context of induced splicing changes. Indeed, a previous study found that MS-275 promotes induction of tumor immune editing of tumor neoantigens and tumor immune

responses in combination with ICI with αPD-1 therapy in bladder cancer (75); however, the doses of MS-275 required to elicit these responses were significantly greater than those used for corin in this study. Importantly, we find that CoREST-regulated splicing factors are overexpressed across many tumor types compared to their respective normal tissues, suggesting that cancer cells are more vulnerable to corin-induced splicing changes due to tumor-associated functions of splicing factors. Given the specific targeting of the CoREST complex by corin and the lack of appreciable in vivo toxicity of corin seen in this study and others[36, 37], we suggest that this work provides a strong preclinical rationale for the use of CoREST inhibitor therapies in combination with ICIs for melanoma and other cancers. Although our findings highlight key tumor-intrinsic effects of corin, future *in vivo* studies should investigate its influence on tumor-extrinsic mechanisms to gain a more comprehensive understanding of how CoREST inhibition shapes tumor-autonomous effects.

Our finding of direct and functionally significant interactions between CoREST and the splicing machinery represents one of the first reports of direct interactions between a histone modifying complex and the splicing machinery. Furthermore, our cryo-EM studies represent, to our knowledge, the first reported structure of a histone modifying complex bound to a splicing factor. Given our findings of CoREST complex interactions with the RNA splicing machinery and its specific regulation of transcription and splicing of pre-mRNA splicing factors, along with previous findings of CoREST complex-mediated post-translational modification of RNA-polymerase II (35), known interactions with transcription factors including SNAG-domain proteins (76) and REST, as well as the BAF complex (42) and CTCF, we propose the following model for CoREST complex regulation of transcription that allows for numerous interacting mechanisms to ensure transcript fidelity, which are disrupted in cancer (**Figure 9**). We suggest that the CoREST complex plays a critical role in ensuring coordinated regulation of chromatin accessibility, transcription factor binding to relevant DNA sites, transcription kinetics and RNA splicing, and that the CoREST

complex provides a means of crosstalk between these systems to ensure proper transcript expression and timing. While we demonstrate the significance of these interactions here in the context of tumorigenesis, we expect these higher order regulatory functions of CoREST, and likely other epigenetic complexes, will prove significant within broader biological processes and provide a critical framework for the tightly coordinated epigenetic control of gene expression.

**METHODS (**Additional details are available in the Supplemental Material)

**Sex as a Biological Variable**

This study exclusively examined female mice. It is unknown whether the findings would be similar for male mice, although we would not expect significant differences.

**Animal Studies**

6-10 week-old female C57BL/6 mice (Jackson Lab) were inoculated with $2.5x10^5$ B16F10 cells. Mice were randomly assigned treatment groups (vehicle control, anti-PD1, corin, and corin + anti-PD1) and treated with 200 µg/mice of corin (HY-111048, MedChemExpress) or 200 µl vehicle control (5% DMSO/PBS) by daily intraperitoneal (i.p.) injections starting from day 6 after the tumor injection. For anti-PD1 treatment, mice were treated with 150 µg/mice anti-PD1 (clone 29F.1A12, BioLegend, 135248) or isotype control (clone RTK2758, BioLegend, 400566) 3 times/week starting from day 7 post-tumor grafts. Treatments occurred blinded and 10 mice per treatment group were used. Tumors were measured 3 times/week and volumes were calculated using the formula V = [1.58π x (length x width)3/2]/6 (77).

**Tissue Processing**

Minced tumor biopsies were incubated with 200µL 20mg/mL collagenase, 200µL 20mg/mL hyaluronidase, and 5µL DNase for 20 minutes to 1 hour with agitation until the tumor fully dissociated. Single-cell suspension was passed through a 100µm strainer and washed with 1X PBS by centrifugation. Cells were resuspended in 1ml of freezing media frozen down.

**Cell lines**

Melanoma cell lines 451Lu, 1205Lu, SKMEL24, WM793, and SKMEL28 were obtained from Meenard Heryln (The Wistar Institute, Philadelphia, Pennsylvania, USA). SKMEL5 cells were obtained from Deborah Lang (Boston University, Boston, Massachusetts, USA). Cells were

maintained at 37C at 5% CO2 and cultured in DMEM (Invitrogen, ThermoFisher Scientific) supplemented with 1% penicillin/streptomycin, L-glutamine (2mM), and 10% FBS. B16F10 cells were cultured in DMEM media (Gibco, 10566024) supplemented with 10% FBS and 100 U/ml of Pen/Strep (Gibco, 15070063). Cells were regularly tested negative for mycoplasma using MycoStrip® - Mycoplasma Detection Kit (InvivoGen, rep-mysnc-50).

**Compounds**

Corin (no. HY-111048), MS275 (etinostat, no. HY-12163), and GSK-LSD1 (HY-100546A) were purchased from MedChemExpress. Stock solutions were made in DMSO and an equivalent volume of DMSO was used as a vehicle control.

**Cryo-EM data collection**

A cryo-EM dataset of truncated LSD1/RCOR1 complex bound to U2AF2 was collected at the Boston University Cryo-EM Core Facility using a 200 kV ThermoFisher Glacios 2 cryoEM microscope equipped with a Falcon 4i direct electron detector and Selectris energy filter. A dataset of 12,845 exposures was collected in counting mode and recorded in Electron Event Representation (EER) format using a magnification of 130kx, pixel size of 0.90 Å, nominal dose of 50 e-/ $Å^2$, dose rate of 10.84 e-/px/s, a defocus range of -1.0 to -2.5 µm, and an energy filter slit width of 10 eV. A multi-shot imaging strategy was used to collect 3 shots per hole, utilizing beam image shift to move between each target.

**RNA-sequencing**

Total RNA was extracted from melanoma cell lines treated with corin or vehicle control (DMSO) using the Qiagen RNeasy Mini Kit. Samples were quantified using nanodrop and sequenced by Azenta Inc.

**Melanoma splicing analysis**

Two tools were used to identify RNA splicing changes from RNA-seq read data. rMATs-turbo (v.4.2.0) (52) was used to call skipped exon, alternative 3'SS, alternative 5'SS, and mutually exclusive events, while AltAnalyze (v.0.7.0.1) (53) was used to call intron retention events. rMATS was run using default parameters for BAM file inputs and the --allow-clipping parameter to prevent soft-clip skipping. A threshold of $q < 0.05$ and deltaPSI $\geq |0.1|$ was used to call significant differential events. AltAnalyze was run using default parameters for BAM file inputs. A threshold of $p < 0.05$ and deltaPSI $\geq |0.1|$ was used to call significant differential events. Gene ontology analysis and visualization was performed on significant SE, RI, and AP events using the R package enrichplot (v.1.22.0). Sashimi plots were generated using rmats2sashimiplot (v.2.0.4).

**RT-PCR splice gels**

Total RNA was extracted using the Qiagen RNeasy Mini Kit. cDNA was synthesized with the SuperScript cDNA Synthesis Kit (ThermoFisher Scientific) and splice products were amplified with splice site-specific primers (**Supplementary Table 10**) and Taq polymerase for 35 cycles at Tm = 52.5C. DNA was run on 1.5% agarose gels and quantified using inclusion:exclusion product ratios.

**Neopeptide prediction analysis**

Two pipelines were used to predict splice-induced neopeptide candidates. First, JCEC files containing significant rMATS SE events ($q < 0.05$, deltaPSI $\geq |0.1|$, $Log2(\text{TPM}) \geq 3$, IJC + SJC $\geq$ 20) were input into SpliceTools (59) to translate and identify peptide sequences produced by frameshifted events. Then, sequences were digested into unique 8-11mer sequences and filtered against the human proteome (UCSC) to isolate neopeptide products. Second, the SNAF (54) T-cell pipeline with default parameters was used to capture additional neopeptides produced from RI, AP, A5'SS, A3'SS, MXE, and trans-splicing events. Predicted neopeptides were validated

against the human proteome and appended to the SpliceTools-identified events. Then, MHC binding predictions were performed using both HLAthena (61) and NetMHCpan (v.4.1) (60) with the following parameters "-l 8, 9, 10, 11" and %Rank $\leq$ 2. Neopeptides identified by both prediction tools were selected and ranked based on a score defined by the product of the -$Log10$(%Rank), junction count, and |deltaPSI| value.

**Candidate neoantigen identification**

Candidate neoantigens were defined based on two methods: 1) a neopeptide was predicted to bind to human MHC and was identified in at least one corin-treated replicate of mass spectrometry (FDR < 0.05) but not in either DMSO-treated replicate 2) a neopeptide was predicted to bind human MHC, had a high rank score (based on deltaPSI, junction count, and binding %Rank, and a high immunogenicity score from DeepImmuno (62) but was not recovered by mass spectrometry as previously described (15,16). Note: C03:04 does not have adequate training data to accurately predict the immunogenicity of bound peptides so only highly ranked A11:01 and B40:01 were tested.

**ELISpot assay**

To expand reactive T cells, HLA-matched PBMCs were pre-stimulated with synthesized peptides (10μg/ml) for 14 days in IL2/IL7 media. APCs were isolated from CD4 and CD8 depleted PBMCs, loaded with peptides (10μg/ml), and seeded at a ratio of 3:1 with the pre-stimulated T cells in a 96 well ELISpot plate. IFN-y ELISpot was performed per manufacturer's instructions and spots were quantified using an Immunospot Analyzer.

**scRNA-seq sample preparation**

Cryopreserved single-suspension tumor samples were thawed and dead cells were removed using the Dead Cell Removal Kit (Miltenyi, 130-090-101) following manufacturer instructions. Live cells from the flow-though were used for CD45+ cell isolation using CD45 mouse MicroBeads (Miltenyi, 130-052-301) following the recommendations. CD45+ cells were counted and resuspended in PBS + 0.04% BSA at 1000 cells/μL for scRNA-seq.

**Statistics**

Results were considered significant for an adjusted *P* value of less than 0.05. Data are presented as the mean ± SD and are representative of at least 2 independent experiments. Tests used to determine statistical significance are noted in the figure legends and include an unpaired, 2-tailed *t* test, a Mann Whitney-U test, 1-way ANOVA with Tukey's test, Holm-Sidak's multiple comparisons test, or a 2-way ANOVA with Tukey's test.

**Study Approval**

Mice were maintained under pathogen-free conditions in an American Association for Accreditation of Laboratory Animal Care (AAALAC)-accredited facility at the Dana Farber Cancer Institute, under the supervision of the Laboratory Animal Science Center (LASC) and its staff of veterinarians and support personnel (IACUC protocol number: 17-014).

**Data and Code Availability**

Raw data, processed data, and metadata from the bulk RNA-seq (GSE280449), scRNA-seq (GSE280450), and PRO-seq (GSE280448) experiments have been deposited in the NCBI's Gene Expression Omnibus (GEO) database. Raw MS data for the CoREST IP-MS are available on PRIDE (project accession: PXD056700, Token: MxX17vDulsT2) and neopeptide IP-MS (MHC associated peptides) are available on the MassIVE public repository (https://massive.ucsd.edu/) under accession code: MSV000096071. All code used for analysis of sequencing were deposited

on GitHub (https://github.com/robertfisher002/CoREST_Splicing; branch main; commit ID 92ac17b). Cryo-EM map and model were deposited in the Protein Data Bank (PDB), EMPAIR database, and Electron Microscopy Data Bank (EMDB) under the following accession codes: (PDB: 9DWU, EMPAIR: 12854, EMDB: 47265). Raw cryo-EM movies will be uploaded to the EMPIAR database. All raw data values can be found in the Supporting Data Values files.

**Acknowledgments:**

The authors would like to thank the Nascent Transcriptomics Core at Harvard Medical School, Boston, MA for performing PRO-seq library construction and for assistance with data analysis, the Center for Macromolecular Interactions at Harvard Medical School for the support with MST experiments, Marianne Collard and Ana Fiszbein for helpful discussions and advice, and members of the BU Department of Dermatology for their helpful suggestions and critical review of this work. The authors would like to thank Dr. Yang Shi (University of Oxford) for generously providing the plasmid encoding His-tagged fl-LSD1.

**Funding Support:**

This work is the result of NIH funding, in whole or in part, and is subject to the NIH Public Access Policy. Through acceptance of this federal funding, the NIH has been given a right to make the work publicly available in PubMed Central.This research was supported by the following: Department of Defense Grant W81XWH2110980 (RMA, KP); Melanoma Research Alliance Grant #1045461 (RMA, RJF); American Heart Association (Postdoctoral Fellowship Award 826614 (K.L.); NIH MIRA grant R35-GM147254 (AF); The Hevolution Foundation (AFAR), the Einstein-Mount Sinai Diabetes Center, and the NIH Office of the Director (S10OD030286) (SS); U01 CA243004 and T32 AI007309-33 (CSE); The Swiss National Science Foundation (Grant 225660) and NIH 1R01CA279391-01A1 (KP); National Institutes of Health grant (R01 CA233800) and the

Masschusetts Life Science Center (JAM); National Institutes of Health grant (GM149229) (PAC); National Institutes of Health grants (U54-CA272688, RO1-HL157174, RO1-CA285308 & RO1-CA279391) (DBK); This work was supported in part by NIH U24CA224331 (to CJW). CJW is the Lavine Family Chair for Preventative Cancer Therapies. Images were created with BioRender.

**Author contributions:**

Conceptualization: RMA, RJF

Methodology: RMA, RJF, KP, KL, KP, AV, CE, PF, SF, JM, HJ, EN, AF, JC, CWH, DBK, SS, CJW, PAC

Investigation: RJF, KP, KL, KP, HJ, EN, AF, AG, ER, CWH, SD, SS

Visualization: RJF, KP, CWH, SS

Funding acquisition: RMA, PAC

Project administration: RMA

Supervision: RMA, PAC, CJW, SS, DBK

Writing – original draft: RMA, RJF

Writing – review & editing: RJF, KP, KL, KP, AV, CE, SF, JM, JC, AG, ER, HJ, EN, AF, CWH, DBK, SS, CJW, PAC, RMA

**Competing interests:** PAC is a founder of Acylin Therapeutics and has been a consultant for Abbvie, Constellation and Epizyme. He is an inventor of an issued U.S. patent for Corin. JAM is a founder, equity holder, and advisor to Entact Bio, serves on the SAB of 908 Devices, and receives or has received sponsored research funding from Vertex, AstraZeneca, Taiho, Springworks, TUO Therapeutics, and Takeda. DBK is a scientific advisor for Immunitrack, a wholly owned subsidiary of Eli Lilly and Company and Breakbio. DBK owns equity in Affimed N.V., Agenus, Armata Pharmaceuticals, Breakbio, BioMarin Pharmaceutical, Celldex Therapeutics, Editas Medicine, Gilead Sciences, Immunitybio, Lexicon Pharmaceuticals. RMA is a co-founder

of Acylin Therapeutics. CJW holds equity at BioNTech, and receives research funding from Pharmacyclics. She is a SAB member of Repertoire, Adventris and Aethon Therapeutics.

## References


1. Baralle FE, Giudice J. Alternative splicing as a regulator of development and tissue identity. *Nat Rev Mol Cell Biol*. 2017;18(7):437-451. doi:10.1038/nrm.2017.27

2. Gallego-Paez LM, Bordone MC, Leote AC, Saraiva-Agostinho N, Ascensão-Ferreira M, Barbosa-Morais NL. Alternative splicing: the pledge, the turn, and the prestige : The key role of alternative splicing in human biological systems. *Hum Genet*. 2017;136(9):1015-1042. doi:10.1007/s00439-017-1790-y

3. Kahles A, Lehmann KV, Toussaint NC, et al. Comprehensive Analysis of Alternative Splicing Across Tumors from 8,705 Patients. *Cancer Cell*. 2018;34(2):211-224.e6. doi:10.1016/j.ccell.2018.07.001

4. Stanley RF, Abdel-Wahab O. Dysregulation and therapeutic targeting of RNA splicing in cancer. *Nat Cancer*. 2022;3(5):536-546. doi:10.1038/s43018-022-00384-z

5. Bradley RK, Anczuków O. RNA splicing dysregulation and the hallmarks of cancer. *Nat Rev Cancer*. 2023;23(3):135-155. doi:10.1038/s41568-022-00541-7

6. Ladomery M. Aberrant alternative splicing is another hallmark of cancer. *Int J Cell Biol*. 2013;2013:463786. doi:10.1155/2013/463786

7. Oltean S, Bates DO. Hallmarks of alternative splicing in cancer. *Oncogene*. 2014;33(46):5311-5318. doi:10.1038/onc.2013.533

8. Desterro J, Bak-Gordon P, Carmo-Fonseca M. Targeting mRNA processing as an anticancer strategy. *Nat Rev Drug Discov*. 2020;19(2):112-129. doi:10.1038/s41573-019-0042-3

9. Siegfried Z, Karni R. The role of alternative splicing in cancer drug resistance. *Curr Opin Genet Dev*. 2018;48:16-21. doi:10.1016/j.gde.2017.10.001

10. Frankiw L, Baltimore D, Li G. Alternative mRNA splicing in cancer immunotherapy. *Nat Rev Immunol*. 2019;19(11):675-687. doi:10.1038/s41577-019-0195-7

11. Park J, Park J, Chung YJ. Alternative splicing: a new breakthrough for understanding tumorigenesis and potential clinical applications. *Genes Genomics*. 2023;45(4):393-400. doi:10.1007/s13258-023-01365-x

12. Jayasinghe RG, Cao S, Gao Q, et al. Systematic Analysis of Splice-Site-Creating Mutations in Cancer. *Cell Rep*. 2018;23(1):270-281.e3. doi:10.1016/j.celrep.2018.03.052

13. Bigot J, Lalanne AI, Lucibello F, et al. Splicing Patterns in SF3B1-Mutated Uveal Melanoma Generate Shared Immunogenic Tumor-Specific Neoepitopes. *Cancer Discov*. 2021;11(8):1938-1951. doi:10.1158/2159-8290.CD-20-0555

14. Oka M, Xu L, Suzuki T, et al. Aberrant splicing isoforms detected by full-length transcriptome sequencing as transcripts of potential neoantigens in non-small cell lung cancer. *Genome Biol*. 2021;22(1):9. doi:10.1186/s13059-020-02240-8

15. Lu SX, De Neef E, Thomas JD, et al. Pharmacologic modulation of RNA splicing enhances anti-tumor immunity. *Cell*. 2021;184(15):4032-4047.e31. doi:10.1016/j.cell.2021.05.038

16. Matsushima S, Ajiro M, Iida K, Chamoto K, Honjo T, Hagiwara M. Chemical induction of splice-neoantigens attenuates tumor growth in a preclinical model of colorectal cancer. *Sci Transl Med*. 2022;14(673):eabn6056. doi:10.1126/scitranslmed.abn6056

17. Xie N, Shen G, Gao W, Huang Z, Huang C, Fu L. Neoantigens: promising targets for cancer therapy. *Signal Transduct Target Ther*. 2023;8(1):9. doi:10.1038/s41392-022-01270-x

18. Bhattacharya S, Levy MJ, Zhang N, et al. The methyltransferase SETD2 couples transcription and splicing by engaging mRNA processing factors through its SHI domain. *Nat Commun*. 2021;12(1):1443. doi:10.1038/s41467-021-21663-w

19. Duan L, Chen Z, Lu J, et al. Histone lysine demethylase KDM4B regulates the alternative splicing of the androgen receptor in response to androgen deprivation. *Nucleic Acids Res*. 2019;47(22):11623-11636. doi:10.1093/nar/gkz1004

20. Gehring NH, Roignant JY. Anything but Ordinary – Emerging Splicing Mechanisms in Eukaryotic Gene Regulation. *Trends Genet*. 2021;37(4):355-372. doi:10.1016/j.tig.2020.10.008

21. Inoue D, Chew GL, Liu B, et al. Spliceosomal disruption of the non-canonical BAF complex in cancer. *Nature*. 2019;574(7778):432-436. doi:10.1038/s41586-019-1646-9

22. Luco RF, Allo M, Schor IE, Kornblihtt AR, Misteli T. Epigenetics in alternative pre-mRNA splicing. *Cell*. 2011;144(1):16-26. doi:10.1016/j.cell.2010.11.056

23. Naftelberg S, Schor IE, Ast G, Kornblihtt AR. Regulation of alternative splicing through coupling with transcription and chromatin structure. *Annu Rev Biochem*. 2015;84:165-198. doi:10.1146/annurev-biochem-060614-034242

24. Shukla S, Kavak E, Gregory M, et al. CTCF-promoted RNA polymerase II pausing links DNA methylation to splicing. *Nature*. 2011;479(7371):74-79. doi:10.1038/nature10442

25. Xiao R, Chen JY, Liang Z, et al. Pervasive Chromatin-RNA Binding Protein Interactions Enable RNA-Based Regulation of Transcription. *Cell*. 2019;178(1):107-121.e18. doi:10.1016/j.cell.2019.06.001

26. Luco RF, Pan Q, Tominaga K, Blencowe BJ, Pereira-Smith OM, Misteli T. Regulation of alternative splicing by histone modifications. *Science*. 2010;327(5968):996-1000. doi:10.1126/science.1184208

27. Luo C, Cheng Y, Liu Y, et al. SRSF2 Regulates Alternative Splicing to Drive Hepatocellular Carcinoma Development. *Cancer Res*. 2017;77(5):1168-1178. doi:10.1158/0008-5472.CAN-16-1919

28. Zhou X, Wang R, Li X, et al. Splicing factor SRSF1 promotes gliomagenesis via oncogenic splice-switching of MYO1B. *J Clin Invest*. 2019;129(2):676-693. doi:10.1172/JCI120279

29. Boddu PC, Gupta A, Roy R, et al. Transcription elongation defects link oncogenic splicing factor mutations to targetable alterations in chromatin landscape. *BioRxiv Prepr Serv Biol*. Published online February 26, 2023:2023.02.25.530019. doi:10.1101/2023.02.25.530019

30. Rahhal R, Seto E. Emerging roles of histone modifications and HDACs in RNA splicing. *Nucleic Acids Res*. 2019;47(10):4911-4926. doi:10.1093/nar/gkz292

31. Burbage M, Rocañín-Arjó A, Baudon B, et al. Epigenetically controlled tumor antigens derived from splice junctions between exons and transposable elements. *Sci Immunol*. 2023;8(80):eabm6360. doi:10.1126/sciimmunol.abm6360

32. Andrés ME, Burger C, Peral-Rubio MJ, et al. CoREST: A functional corepressor required for regulation of neural-specific gene expression. *Proc Natl Acad Sci*. 1999;96(17):9873-9878. doi:10.1073/pnas.96.17.9873

33. Lee K, Whedon SD, Wang ZA, Cole PA. Distinct biochemical properties of the class I histone deacetylase complexes. *Curr Opin Chem Biol*. 2022;70:102179. doi:10.1016/j.cbpa.2022.102179

34. Wang ZA, Millard CJ, Lin CL, et al. Diverse nucleosome Site-Selectivity among histone deacetylase complexes. *eLife*. 2020;9:e57663. doi:10.7554/eLife.57663

35. Rivera C, Lee HG, Lappala A, et al. Unveiling RCOR1 as a rheostat at transcriptionally permissive chromatin. *Nat Commun*. 2022;13(1):1550. doi:10.1038/s41467-022-29261-0

36. Kalin JH, Wu M, Gomez AV, et al. Targeting the CoREST complex with dual histone deacetylase and demethylase inhibitors. *Nat Commun*. 2018;9(1):53. doi:10.1038/s41467-017-02242-4

37. Wu M, Hanly A, Gibson F, et al. The CoREST Repressor Complex Mediates Phenotype Switching and Therapy Resistance in Melanoma. *bioRxiv*. Published online 2020:2020.09.30.320580. doi:10.1101/2020.09.30.320580

38. Anastas JN, Zee BM, Kalin JH, et al. Re-programing Chromatin with a Bifunctional LSD1/HDAC Inhibitor Induces Therapeutic Differentiation in DIPG. *Cancer Cell*. 2019;36(5):528-544.e10. doi:10.1016/j.ccell.2019.09.005

39. Soukar I, Fisher R, Bhagavatula S, Collard M, Cole PA, Alani RM. The CoREST complex is a therapeutic vulnerability in malignant peripheral nerve sheath tumors. *BioRxiv Prepr Serv Biol*. Published online August 19, 2024:2024.08.17.607802. doi:10.1101/2024.08.17.607802

40. Miller SA, Policastro RA, Savant SS, et al. Lysine-Specific Demethylase 1 Mediates AKT Activity and Promotes Epithelial-to-Mesenchymal Transition in PIK3CA-Mutant Colorectal Cancer. *Mol Cancer Res MCR*. 2020;18(2):264-277. doi:10.1158/1541-7786.MCR-19-0748

41. Asmamaw MD, He A, Zhang LR, Liu HM, Gao Y. Histone deacetylase complexes: Structure, regulation and function. *Biochim Biophys Acta Rev Cancer*. 2024;1879(5):189150. doi:10.1016/j.bbcan.2024.189150

42. Garcia-Martinez L, Adams AM, Chan HL, et al. Endocrine resistance and breast cancer plasticity are controlled by CoREST. *Nat Struct Mol Biol*. 2022;29(11):1122-1135. doi:10.1038/s41594-022-00856-x

43. Das S, Krainer AR. Emerging functions of SRSF1, splicing factor and oncoprotein, in RNA metabolism and cancer. *Mol Cancer Res MCR*. 2014;12(9):1195-1204. doi:10.1158/1541-7786.MCR-14-0131

44. Larsson CA, Cote G, Quintás-Cardama A. The changing mutational landscape of acute myeloid leukemia and myelodysplastic syndrome. *Mol Cancer Res MCR*. 2013;11(8):815-827. doi:10.1158/1541-7786.MCR-12-0695

45. Abramson J, Adler J, Dunger J, et al. Accurate structure prediction of biomolecular interactions with AlphaFold 3. *Nature*. 2024;630(8016):493-500. doi:10.1038/s41586-024-07487-w

46. Forneris F, Binda C, Adamo A, Battaglioli E, Mattevi A. Structural basis of LSD1-CoREST selectivity in histone H3 recognition. *J Biol Chem*. 2007;282(28):20070-20074. doi:10.1074/jbc.C700100200

47. Kim SA, Zhu J, Yennawar N, Eek P, Tan S. Crystal Structure of the LSD1/CoREST Histone Demethylase Bound to Its Nucleosome Substrate. *Mol Cell*. 2020;78(5):903-914.e4. doi:10.1016/j.molcel.2020.04.019

48. Maji D, Glasser E, Henderson S, et al. Representative cancer-associated U2AF2 mutations alter RNA interactions and splicing. *J Biol Chem*. 2020;295(50):17148-17157. doi:10.1074/jbc.RA120.015339

49. Glasser E, Maji D, Biancon G, et al. Pre-mRNA splicing factor U2AF2 recognizes distinct conformations of nucleotide variants at the center of the pre-mRNA splice site signal. *Nucleic Acids Res*. 2022;50(9):5299-5312. doi:10.1093/nar/gkac287

50. Bonnal SC, López-Oreja I, Valcárcel J. Roles and mechanisms of alternative splicing in cancer — implications for care. *Nat Rev Clin Oncol*. 2020;17(8):457-474. doi:10.1038/s41571-020-0350-x

51. Arozarena I, Wellbrock C. Phenotype plasticity as enabler of melanoma progression and therapy resistance. *Nat Rev Cancer*. 2019;19(7):377-391. doi:10.1038/s41568-019-0154-4

52. Wang Y, Xie Z, Kutschera E, Adams JI, Kadash-Edmondson KE, Xing Y. rMATS-turbo: an efficient and flexible computational tool for alternative splicing analysis of large-scale RNA-seq data. *Nat Protoc*. 2024;19(4):1083-1104. doi:10.1038/s41596-023-00944-2

53. Emig D, Salomonis N, Baumbach J, Lengauer T, Conklin BR, Albrecht M. AltAnalyze and DomainGraph: analyzing and visualizing exon expression data. *Nucleic Acids Res*. 2010;38(Web Server issue):W755-762. doi:10.1093/nar/gkq405

54. Li G, Mahajan S, Ma S, et al. Splicing neoantigen discovery with SNAF reveals shared targets for cancer immunotherapy. *Sci Transl Med*. 2024;16(730):eade2886. doi:10.1126/scitranslmed.ade2886

55. Rybak JN, Roesli C, Kaspar M, Villa A, Neri D. The extra-domain A of fibronectin is a vascular marker of solid tumors and metastases. *Cancer Res*. 2007;67(22):10948-10957. doi:10.1158/0008-5472.CAN-07-1436

56. Kim YE, Won M, Lee SG, Park C, Song CH, Kim KK. RBM47-regulated alternative splicing of TJP1 promotes actin stress fiber assembly during epithelial-to-mesenchymal transition. *Oncogene*. 2019;38(38):6521-6536. doi:10.1038/s41388-019-0892-5

57. Zhang Y, Yao X, Zhou H, et al. OncoSplicing: an updated database for clinically relevant alternative splicing in 33 human cancers. *Nucleic Acids Res*. 2022;50(D1):D1340-D1347. doi:10.1093/nar/gkab851

58. Geethadevi A, Vaidya N, Fisher RJ, et al. The CoREST complex inhibitor, corin, leads to decreased tumor growth, increased cellular differentiation and extended lifespan in atypical teratoid rhabdoid tumor xenograft models. Preprint posted online December 17, 2024. doi:10.1101/2024.12.14.628381

59. Flemington EK, Flemington SA, O'Grady TM, et al. SpliceTools, a suite of downstream RNA splicing analysis tools to investigate mechanisms and impact of alternative splicing. *Nucleic Acids Res*. 2023;51(7):e42-e42. doi:10.1093/nar/gkad111

60. Reynisson B, Alvarez B, Paul S, Peters B, Nielsen M. NetMHCpan-4.1 and NetMHCIIpan-4.0: improved predictions of MHC antigen presentation by concurrent motif deconvolution and integration of MS MHC eluted ligand data. *Nucleic Acids Res*. 2020;48(W1):W449-W454. doi:10.1093/nar/gkaa379

61. Sarkizova S, Klaeger S, Le PM, et al. A large peptidome dataset improves HLA class I epitope prediction across most of the human population. *Nat Biotechnol*. 2020;38(2):199-209. doi:10.1038/s41587-019-0322-9

62. Li G, Iyer B, Prasath VBS, Ni Y, Salomonis N. DeepImmuno: deep learning-empowered prediction and generation of immunogenic peptides for T-cell immunity. *Brief Bioinform*. 2021;22(6):bbab160. doi:10.1093/bib/bbab160

63. Aran D, Looney AP, Liu L, et al. Reference-based analysis of lung single-cell sequencing reveals a transitional profibrotic macrophage. *Nat Immunol*. 2019;20(2):163-172. doi:10.1038/s41590-018-0276-y

64. Floro J, Dai A, Metzger A, et al. SDE2 is an essential gene required for ribosome biogenesis and the regulation of alternative splicing. *Nucleic Acids Res*. 2021;49(16):9424-9443. doi:10.1093/nar/gkab647

65. Shen SM, Ji Y, Zhang C, et al. Nuclear PTEN safeguards pre-mRNA splicing to link Golgi apparatus for its tumor suppressive role. *Nat Commun*. 2018;9(1):2392. doi:10.1038/s41467-018-04760-1

66. Glasser E, Agrawal AA, Jenkins JL, Kielkopf CL. Cancer-Associated Mutations Mapped on High-Resolution Structures of the U2AF2 RNA Recognition Motifs. *Biochemistry*. 2017;56(36):4757-4761. doi:10.1021/acs.biochem.7b00551

67. Kang HS, Sánchez-Rico C, Ebersberger S, et al. An autoinhibitory intramolecular interaction proof-reads RNA recognition by the essential splicing factor U2AF2. *Proc Natl Acad Sci U S A*. 2020;117(13):7140-7149. doi:10.1073/pnas.1913483117

68. Schneider-Poetsch T, Chhipi-Shrestha JK, Yoshida M. Splicing modulators: on the way from nature to clinic. *J Antibiot (Tokyo)*. 2021;74(10):603-616. doi:10.1038/s41429-021-00450-1

69. Feustel K, Falchook GS. Protein Arginine Methyltransferase 5 (PRMT5) Inhibitors in Oncology Clinical Trials: A review. *J Immunother Precis Oncol*. 2022;5(3):58-67. doi:10.36401/JIPO-22-1

70. Hwang JW, Cho Y, Bae GU, Kim SN, Kim YK. Protein arginine methyltransferases: promising targets for cancer therapy. *Exp Mol Med*. 2021;53(5):788-808. doi:10.1038/s12276-021-00613-y

71. Westcott PMK, Sacks NJ, Schenkel JM, et al. Low neoantigen expression and poor T-cell priming underlie early immune escape in colorectal cancer. *Nat Cancer*. 2021;2(10):1071-1085. doi:10.1038/s43018-021-00247-z

72. Samstein RM, Lee CH, Shoushtari AN, et al. Tumor mutational load predicts survival after immunotherapy across multiple cancer types. *Nat Genet*. 2019;51(2):202-206. doi:10.1038/s41588-018-0312-8

73. Topalian SL, Forde PM, Emens LA, Yarchoan M, Smith KN, Pardoll DM. Neoadjuvant immune checkpoint blockade: A window of opportunity to advance cancer immunotherapy. *Cancer Cell*. 2023;41(9):1551-1566. doi:10.1016/j.ccell.2023.07.011

74. Palmeri M, Mehnert J, Silk AW, et al. Real-world application of tumor mutational burden-high (TMB-high) and microsatellite instability (MSI) confirms their utility as immunotherapy biomarkers. *ESMO Open*. 2022;7(1):100336. doi:10.1016/j.esmoop.2021.100336

75. Truong AS, Zhou M, Krishnan B, et al. Entinostat induces antitumor immune responses through immune editing of tumor neoantigens. *J Clin Invest*. 2021;131(16):e138560. doi:10.1172/JCI138560

76. van Bergen MGJM, van der Reijden BA. Targeting the GFI1/1B-CoREST Complex in Acute Myeloid Leukemia. *Front Oncol*. 2019;9:1027. doi:10.3389/fonc.2019.01027

77. Feldman J, Goldwasser R, Mark S, Schwartz J, Orion I. A Mathematical Model for Tumor Volume Evaluation using Two-Dimensions. *J Appl Quanitative Methods*. 2009;4(4).

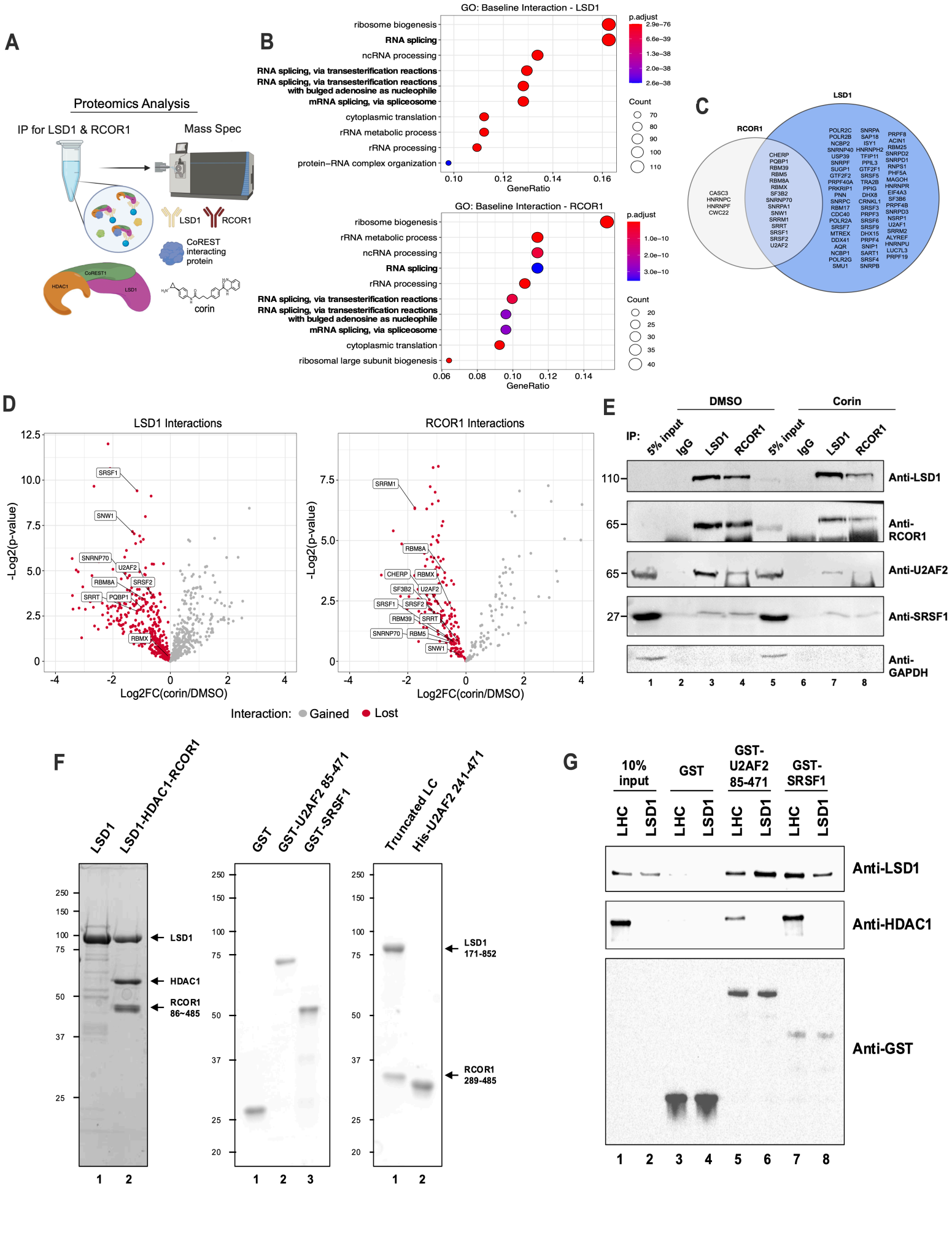
A
Proteomics Analysis
IP for LSD1 & RCOR1
Mass Spec
LSD1
RCOR1
CoREST interacting protein
HDAC1
CoREST1
LSD1
corin
B
GO: Baseline Interaction - LSD1
ribosome biogenesis
RNA splicing
ncRNA processing
RNA splicing, via transesterification reactions
RNA splicing, via transesterification reactions with bulged adenosine as nucleophile
mRNA splicing, via spliceosome
cytoplasmic translation
rRNA metabolic process
rRNA processing
protein–RNA complex organization
0.10
0.12
0.14
0.16
GeneRatio
p.adjust
2.9e-76
6.6e-39
1.3e-38
2.0e-38
2.6e-38
Count
70
80
90
100
110
GO: Baseline Interaction - RCOR1
ribosome biogenesis
rRNA metabolic process
ncRNA processing
RNA splicing
rRNA processing
RNA splicing, via transesterification reactions
RNA splicing, via transesterification reactions with bulged adenosine as nucleophile
mRNA splicing, via spliceosome
cytoplasmic translation
ribosomal large subunit biogenesis
0.06
0.08
0.10
0.12
0.14
GeneRatio
p.adjust
1.0e-10
2.0e-10
3.0e-10
Count
20
25
30
35
40
C
LSD1
RCOR1
CASC3
HNRNPC
HNRNPF
CWC22
CHERP
PQBP1
RBM39
RBM5
RBM8A
RBMX
SF3B2
SNRNP70
SNRPA1
SNW1
SRRM1
SRRT
SRSF1
SRSF2
U2AF2
POLR2C
POLR2B
NCBP2
SNRNP40
USP39
SNRPF
SUGP1
GTF2F2
PRPF40A
PRKRIP1
PNN
SNRPC
RBM17
CDC40
POLR2A
SRSF7
MTREX
DDX41
AQR
NCBP1
POLR2G
SMU1
SNRPA
SAP18
ISY1
HNRNPH2
TFIP11
PPIL3
GTF2F1
SRSF5
TRA2B
PPIG
DHX8
CRNKL1
SRSF3
PRPF3
SRSF6
SRSF9
DHX15
PRPF4
SNIP1
SART1
SRSF4
SNRPB
PRPF8
ACIN1
RBM25
SNRPD2
SNRPD1
RNPS1
PHF5A
MAGOH
HNRNPR
EIF4A3
SF3B6
PRPF4B
SNRPD3
NSRP1
U2AF1
SRRM2
ALYREF
HNRNPU
LUC7L3
PRPF19
D
LSD1 Interactions
RCOR1 Interactions
-Log2(p-value)
Log2FC(corin/DMSO)
SRSF1
SNW1
SNRNP70
U2AF2
RBM8A
SRSF2
SRRT
PQBP1
RBMX
SRRM1
CHERP
SF3B2
Interaction: Gained Lost
E
DMSO
Corin
IP:
5% input
IgG
LSD1
RCOR1
Anti-LSD1
Anti-RCOR1
Anti-U2AF2
Anti-SRSF1
Anti-GAPDH
110
65
27
1 2 3 4 5 6 7 8
F
LSD1
LSD1-HDAC1-RCOR1
LSD1
HDAC1
RCOR1 86~485
GST
GST-U2AF2 85-471
GST-SRSF1
Truncated LC
His-U2AF2 241-471
LSD1 171-852
RCOR1 289-485
250
150
100
75
50
37
25
20
1 2
1 2 3
1 2
G
10% input
GST
GST-U2AF2 85-471
GST-SRSF1
LHC
LSD1
Anti-LSD1
Anti-HDAC1
Anti-GST
1 2 3 4 5 6 7 8

**Figure 1. The CoREST complex interacts with splicing factors. (A)** Overview of immunoprecipitation-mass spectrometry experiment completed in duplicate. **(B)** Gene ontology analysis for proteins found to have significant baseline interactions (LogFC > 1, $p < 0.05$) with LSD1 (top) and RCOR1 (bottom). Enrichment analysis was performed using the hypergeometric test with multiple test correction by the Benjamini-Hochberg method. **(C)** Venn diagram of RNA splicing proteins found to significantly interact with LSD1 and RCOR1. **(D)** Volcano plots of LSD1 (left) and RCOR1 (right) baseline interactions lost with corin treatment (red). Labelled points are proteins from the overlap in (C). Statistical anlaysis was performed using the heteroscedastic t-test. **(E)** IP-WB analysis of CoREST complex-U2AF2 and CoREST complex-SRSF1 interactions with DMSO or corin treatment (24h, 2.5μM). **(F)** SDS-PAGE and Coomassie Blue staining of purified proteins. **(G)** GST pull-down assay using purified GST-tagged U2AF2 (amino acids 85–471) or SRSF1, and purified CoREST complex (LHC) or LSD1 protein.

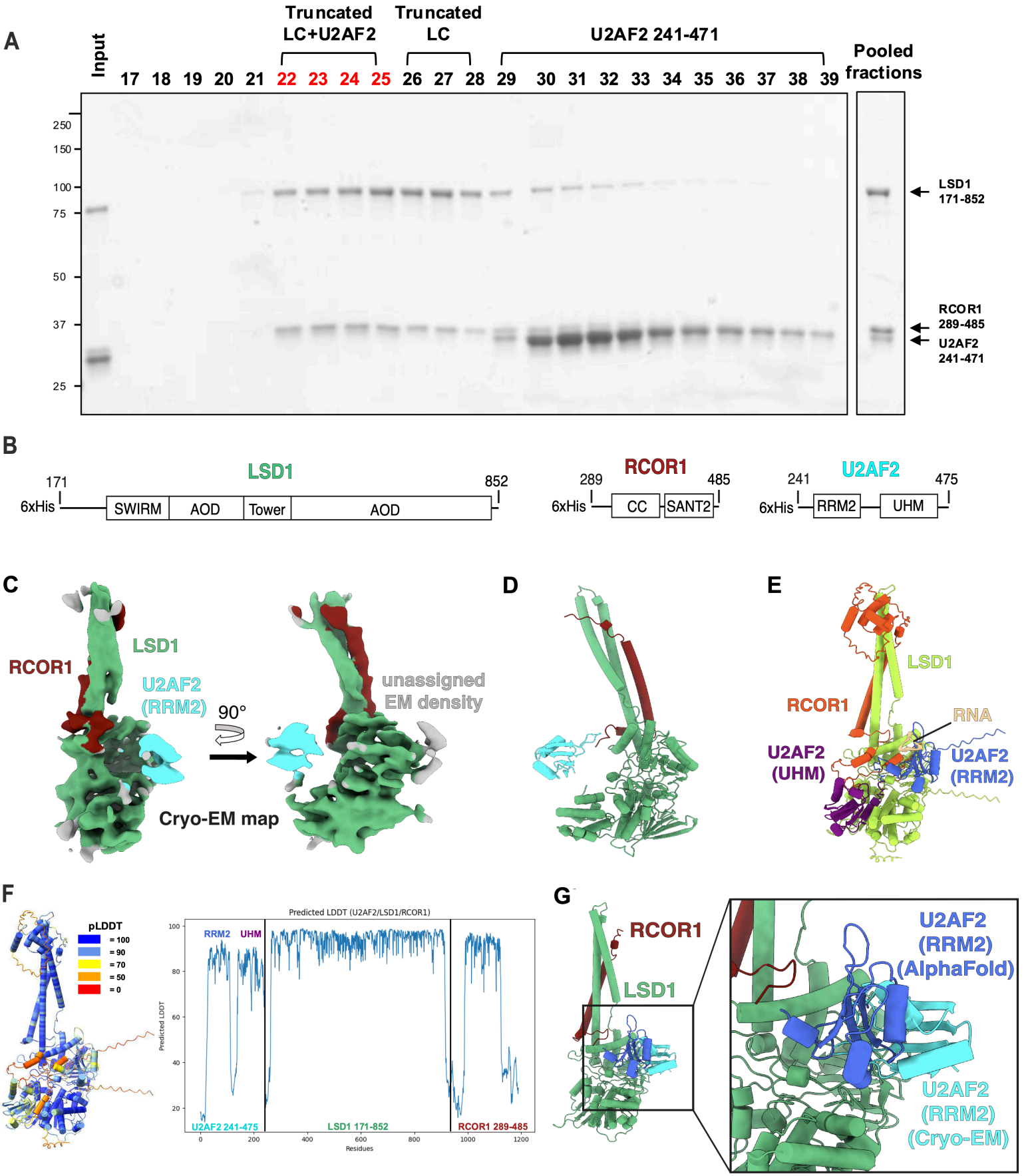
A
Input
Truncated LC+U2AF2
Truncated LC
U2AF2 241-471
Pooled fractions
17 18 19 20 21 22 23 24 25 26 27 28 29 30 31 32 33 34 35 36 37 38 39
250
150
100
75
50
37
25
LSD1 171-852
RCOR1 289-485
U2AF2 241-471
B
LSD1
171
6xHis
SWIRM
AOD
Tower
AOD
852
RCOR1
289
6xHis
CC
SANT2
485
U2AF2
241
6xHis
RRM2
UHM
475
C
RCOR1
LSD1
U2AF2 (RRM2)
90°
unassigned EM density
Cryo-EM map
D
E
LSD1
RCOR1
RNA
U2AF2 (UHM)
U2AF2 (RRM2)
F
pLDDT
= 100
= 90
= 70
= 50
= 0
Predicted LDDT (U2AF2/LSD1/RCOR1)
RRM2
UHM
U2AF2 241-475
LSD1 171-852
RCOR1 289-485
Predicted LDDT
Residues
G
RCOR1
LSD1
U2AF2 (RRM2) (AlphaFold)
U2AF2 (RRM2) (Cryo-EM)

**Figure 2. Cryo-EM structure and AlphaFold prediction of U2AF2 bound to LSD1+RCOR1.** **(A)** Size exclusion chromatography for cryo-EM sample preparation. The early fractions (fractions 22–25), containing LSD1, RCOR1, and U2AF2, were pooled, concentrated and subsequently used for cryo-EM analysis. **(B)** Domain schematic of all protein components used for cryo-EM sample preparation. **(C)** Cryo-EM map of the RRM2 domain of U2AF2 bound to the LSD1+RCOR1 complex. **(D)** Cryo-EM model in cartoon view representing the cryo-EM map shown in panel (C). (**E**) AlphaFold model representing the prediction shown in panel (D). **(F)** Predicted local distance difference test (pLDDT) plot of the AlphaFold multimer prediction incorporating LSD1, RCOR1, U2AF2, and RNA. **(G)** Superimposition of the RRM2 domain of U2AF2 from AlphaFold multimer over our cryo-EM structure of LSD1+RCOR1+U2AF2. Zoomed-in box shows the degree of similarity in position between the two RRM2 globular domain models.

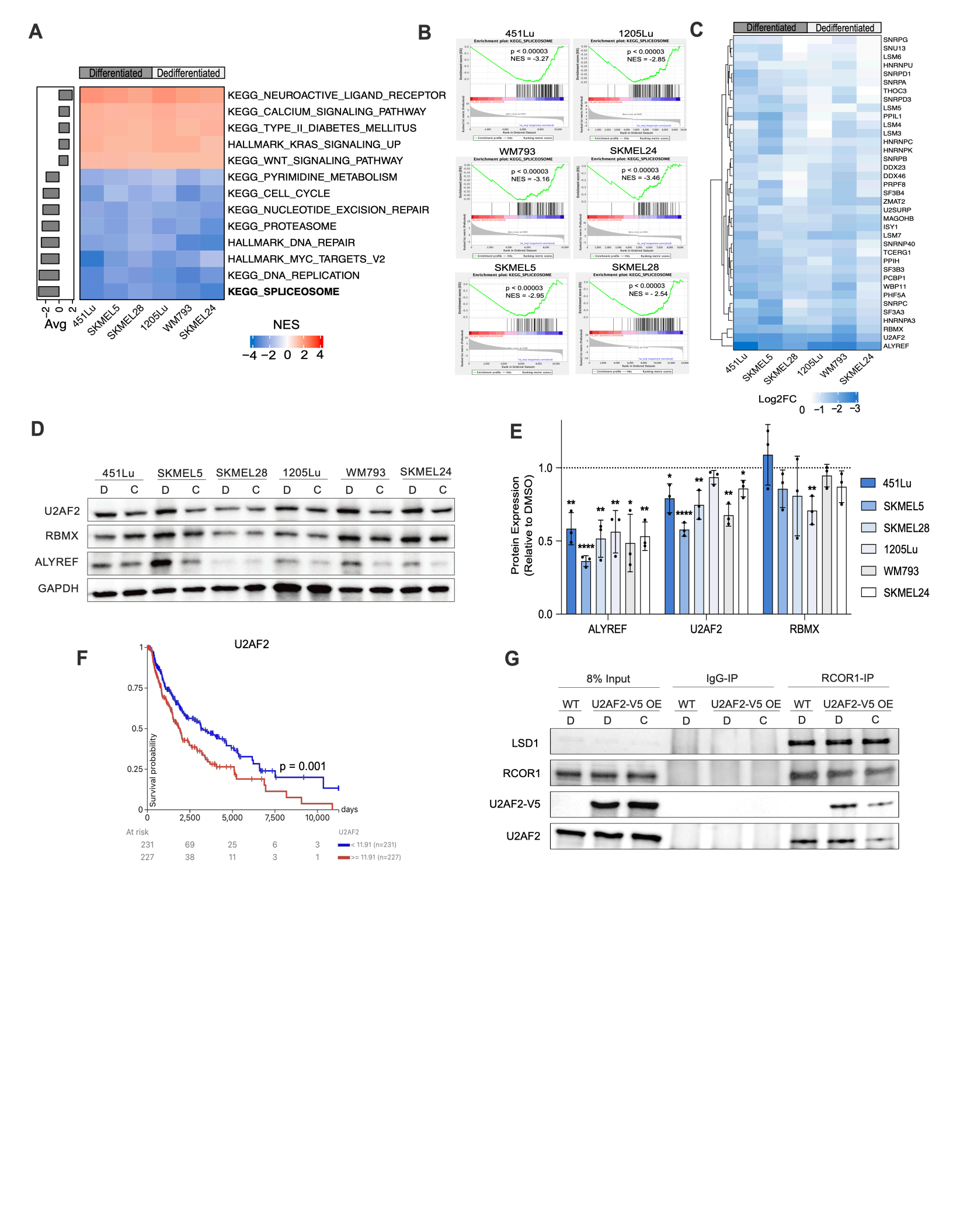
A
Differentiated
Dedifferentiated
KEGG_NEUROACTIVE_LIGAND_RECEPTOR
KEGG_CALCIUM_SIGNALING_PATHWAY
KEGG_TYPE_II_DIABETES_MELLITUS
HALLMARK_KRAS_SIGNALING_UP
KEGG_WNT_SIGNALING_PATHWAY
KEGG_PYRIMIDINE_METABOLISM
KEGG_CELL_CYCLE
KEGG_NUCLEOTIDE_EXCISION_REPAIR
KEGG_PROTEASOME
HALLMARK_DNA_REPAIR
HALLMARK_MYC_TARGETS_V2
KEGG_DNA_REPLICATION
KEGG_SPLICEOSOME
Avg
451Lu
SKMEL5
SKMEL28
1205Lu
WM793
SKMEL24
NES
−4 −2 0 2 4
B
451Lu
1205Lu
WM793
SKMEL24
SKMEL5
SKMEL28
p < 0.00003
NES = -3.27
NES = -2.85
NES = -3.16
NES = -3.46
NES = -2.95
NES = - 2.54
C
Differentiated
Dedifferentiated
SNRPG
SNU13
LSM6
HNRNPU
SNRPD1
SNRPA
THOC3
SNRPD3
LSM5
PPIL1
LSM4
LSM3
HNRNPC
HNRNPK
SNRPB
DDX23
DDX46
PRPF8
SF3B4
ZMAT2
U2SURP
MAGOHB
ISY1
LSM7
SNRNP40
TCERG1
PPIH
SF3B3
PCBP1
WBP11
PHF5A
SNRPC
SF3A3
HNRNPA3
RBMX
U2AF2
ALYREF
Log2FC
0 −1 −2 −3
D
451Lu
SKMEL5
SKMEL28
1205Lu
WM793
SKMEL24
D C
U2AF2
RBMX
ALYREF
GAPDH
E
Protein Expression
(Relative to DMSO)
1.0
0.5
0.0
ALYREF
U2AF2
RBMX
451Lu
SKMEL5
SKMEL28
1205Lu
WM793
SKMEL24
F
U2AF2
Survival probability
p = 0.001
days
At risk
U2AF2
231 69 25 6 3
< 11.91 (n=231)
227 38 11 3 1
>= 11.91 (n=227)
G
8% Input
IgG-IP
RCOR1-IP
WT
U2AF2-V5 OE
D C
LSD1
RCOR1
U2AF2-V5
U2AF2

**Figure 3. CoREST transcriptionally regulates splicing factor gene expression. (A)** Heatmap of significant KEGG and Hallmark pathways ($p < 0.05$) across six melanoma cell lines treated with corin (24h, 2.5μM) in duplicate. Pathways are ranked by average normalized enrichment score (NES) and cell lines are grouped based on phenotype. **(B)** Gene Set Enrichment Analysis plots for each cell line showing a significant negative enrichment for "KEGG Spliceosome". **(C)** Heatmap of splicing factor genes significantly downregulated by corin treatment ($q < 0.01$, $Log2FC < -0.5$) across all six melanoma cell lines clustered using Euclidean distance. **(D)** Representative western blot of downregulated splicing factors across six melanoma cell lines treated with DMSO (D) or corin (C) and quantification of biological replicates (n =3) **(E).** Error bars represent the standard deviation (SD). **(F)** Kaplan-Meier plot of TCGA-SKCM patient survival based on median U2AF2 expression. Significance was determined using a log-rank test. **(g)** IP-WB analysis of CoREST-U2AF2 interactions following DMSO (D) and corin (C) treatment (24h, 2.5μM) in V5-tagged U2AF2 overexpression SKMEL5 cells**.**

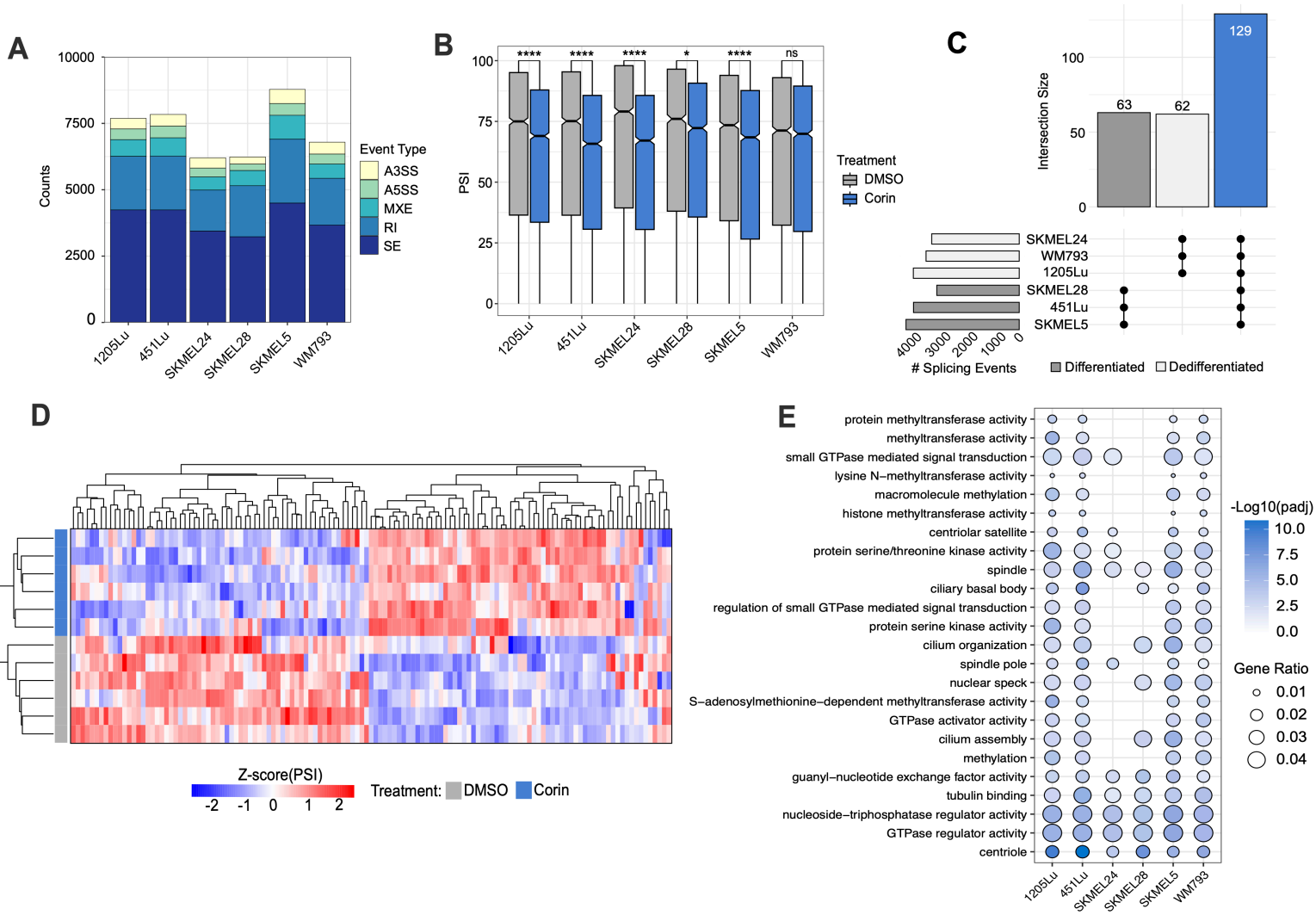
A
Counts
Event Type
A3SS
A5SS
MXE
RI
SE
1205Lu
451Lu
SKMEL24
SKMEL28
SKMEL5
WM793
B
PSI
Treatment
DMSO
Corin
****
****
****
*
****
ns
C
Intersection Size
63
62
129
# Splicing Events
Differentiated
Dedifferentiated
D
Z-score(PSI)
Treatment: DMSO Corin
E
protein methyltransferase activity
methyltransferase activity
small GTPase mediated signal transduction
lysine N−methyltransferase activity
macromolecule methylation
histone methyltransferase activity
centriolar satellite
protein serine/threonine kinase activity
spindle
ciliary basal body
regulation of small GTPase mediated signal transduction
protein serine kinase activity
cilium organization
spindle pole
nuclear speck
S−adenosylmethionine−dependent methyltransferase activity
GTPase activator activity
cilium assembly
methylation
guanyl−nucleotide exchange factor activity
tubulin binding
nucleoside−triphosphatase regulator activity
GTPase regulator activity
centriole
-Log10(padj)
Gene Ratio

**Figure 4. Corin induces RNA splicing changes in melanoma. (A)** Summary of significant RNA splicing changes across six melanoma cell lines treated with corin (deltaPSI $\geq$ |0.1|, q < 0.05) in duplicate. **(B)** Percent Spliced In (PSI) levels for all significant SE events following DMSO and corin treatment. Statistical comparisons were performed using a two-sample t-test to assess differences in PSI value between treatment groups within each cell line. P-values were adjusted for multiple comparisons using the Bonferroni correction (*p.adj < 0.05, **p.adj < 0.01, ***p.adj < 0.001, ****p.adj < 0.0001). **(C)** UpSet plot of skipped exon (SE) events that are exclusive to the differentiated phenotype, dedifferentiated phenotype, or shared by all cell lines (blue). **(D)** Unsupervised hierarchical clustering heatmap based on Euclidian distance of shared skipped exon inclusion levels. Rows are melanoma cell lines clustered by treatment and columns are shared inclusion events. **(E)** Gene ontology dotplot of the top pathways impacted by corin-induced differential exon inclusion across all cell lines (median padj < 0.01). Enrichment analysis was performed using the hypergeometric test with multiple test correction by the Benjamini-Hochberg method.

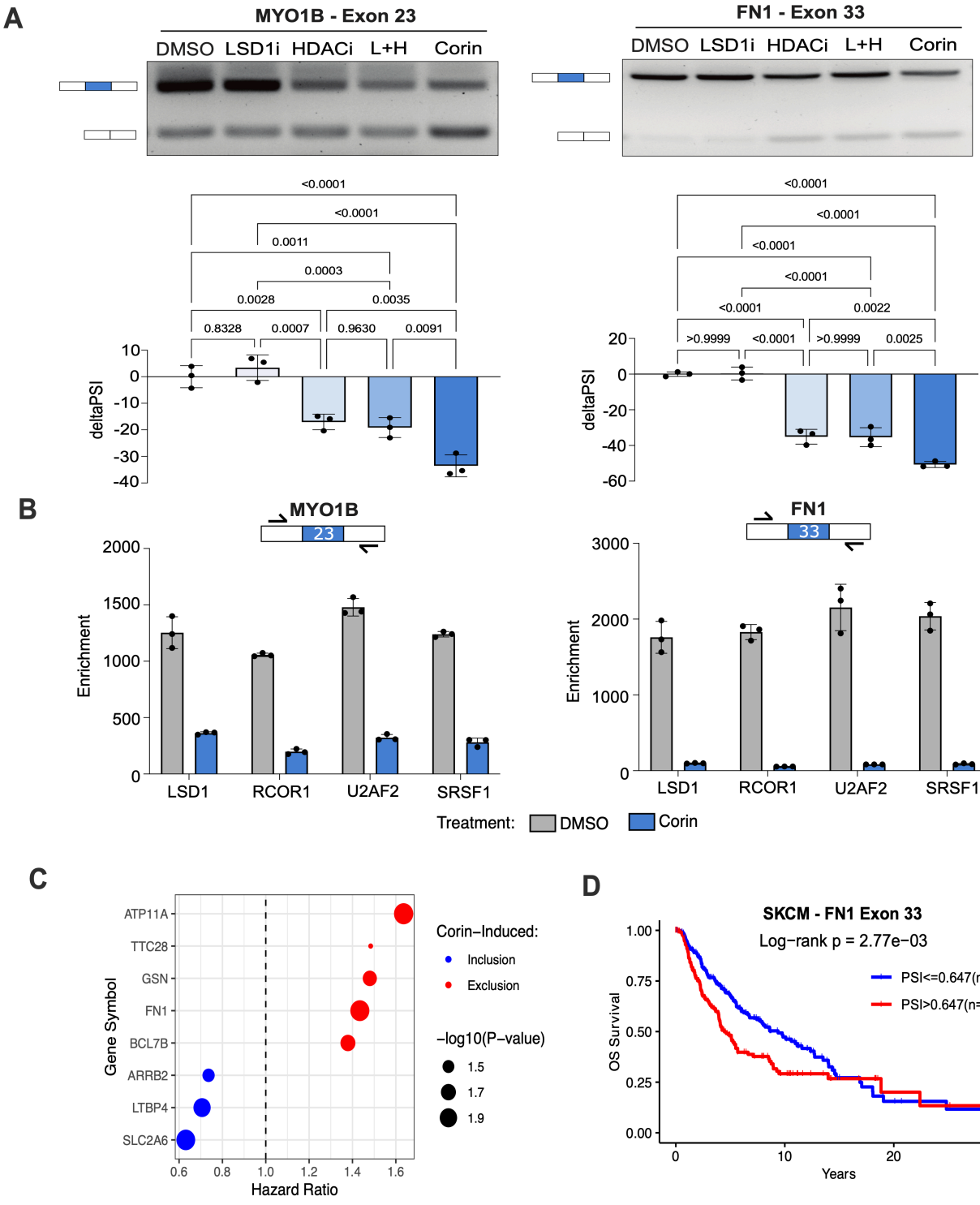
A
MYO1B - Exon 23
DMSO LSD1i HDACi L+H Corin
FN1 - Exon 33
DMSO LSD1i HDACi L+H Corin
deltaPSI
B
MYO1B
FN1
Enrichment
LSD1
RCOR1
U2AF2
SRSF1
Treatment: DMSO Corin
C
Gene Symbol
ATP11A
TTC28
GSN
FN1
BCL7B
ARRB2
LTBP4
SLC2A6
Hazard Ratio
Corin−Induced:
Inclusion
Exclusion
−log10(P−value)
D
SKCM - FN1 Exon 33
Log−rank p = 2.77e−03
PSI<=0.647(n=227)
PSI>0.647(n=223)
OS Survival
Years

**Figure 5. Corin induces splicing events associated with melanoma survival.**

**. (A)** Representative RT-PCR gels and quantification comparing corin to single agent inhibitors of HDAC and LSD1 in MYO1B and FN1 splicing. Statistical analysis of biological replicates (n=3) was performed using a one-way ANOVA with Tukey's post hoc test for multiple comparisons. Error bars represent the standard deviation (SD). **(B)** Representative RIP-qPCR biological replicate (n=2) with 3 technical replicates of CoREST complex subunits and splicing factor occupancy at MYO1B and FN1 splice sites with corin treatment. Error bars represent the standard deviation (SD). **(C)** Hazard ratios for corin-induced splicing events based on TCGA-SKCM survival data measured using the Cox proportional hazards regression. **(D)** Kaplan-Meier curve of FN1 exon 33 inclusion in TCGA-SKCM using the median PSI threshold. Significance was determined using a log-rank test.

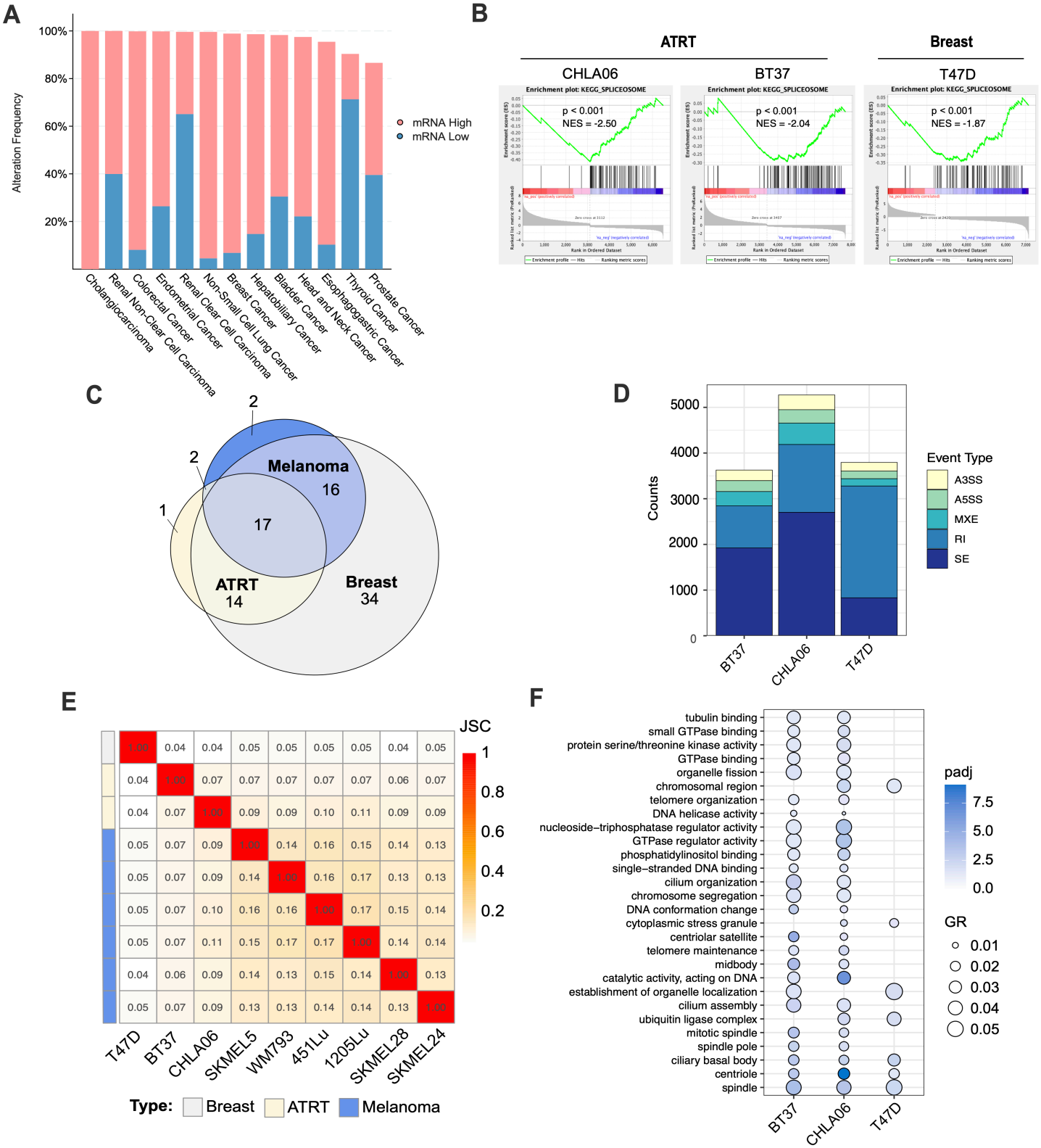
A
100%
80%
60%
40%
20%
Alteration Frequency
mRNA High
mRNA Low
Cholangiocarcinoma
Renal Non-Clear Cell Carcinoma
Colorectal Cancer
Endometrial Cancer
Renal Clear Cell Carcinoma
Non-Small Cell Lung Cancer
Breast Cancer
Hepatobiliary Cancer
Bladder Cancer
Head and Neck Cancer
Esophagogastric Cancer
Thyroid Cancer
Prostate Cancer
B
ATRT
Breast
CHLA06
BT37
T47D
Enrichment plot: KEGG_SPLICEOSOME
p < 0.001
NES = -2.50
p < 0.001
NES = -2.04
p < 0.001
NES = -1.87
C
Melanoma
16
17
ATRT
14
Breast
34
2
2
1
D
Counts
5000
4000
3000
2000
1000
0
BT37
CHLA06
T47D
Event Type
A3SS
A5SS
MXE
RI
SE
E
JSC
1
0.8
0.6
0.4
0.2
T47D
BT37
CHLA06
SKMEL5
WM793
451Lu
1205Lu
SKMEL28
SKMEL24
Type:
Breast
ATRT
Melanoma
F
tubulin binding
small GTPase binding
protein serine/threonine kinase activity
GTPase binding
organelle fission
chromosomal region
telomere organization
DNA helicase activity
nucleoside−triphosphatase regulator activity
GTPase regulator activity
phosphatidylinositol binding
single−stranded DNA binding
cilium organization
chromosome segregation
DNA conformation change
cytoplasmic stress granule
centriolar satellite
telomere maintenance
midbody
catalytic activity, acting on DNA
establishment of organelle localization
cilium assembly
ubiquitin ligase complex
mitotic spindle
spindle pole
ciliary basal body
centriole
spindle
BT37
CHLA06
T47D
padj
7.5
5.0
2.5
0.0
GR
0.01
0.02
0.03
0.04
0.05

**Figure 6. Corin impacts RNA splicing across cancers. (A)** Histogram depicting the frequency of altered mRNA expression alteration in CoREST complex-regulated RNA splicing factors between cancer and matched normal tissue from cBioPortal stratified by cancer type. Pink bars indicate the frequency of overexpression events and blue bars indicate the frequency of downregulation events. **(B)** Gene Set Enrichment Analysis plots for "KEGG Spliceosome" in ATRT and breast cancer cell lines treated with corin. **(C)** Venn diagram of splicing factors significantly downregulated by corin in melanoma, ATRT, and breast cancer. **(D)** Summary of corin-induced RNA splicing changes in ATRT and breast cancer cells. **(E)** Jaccard similarity index comparing corin-induced splicing events across all cell lines and cancer types. **(F)** Gene ontology analysis of common significant pathways affected by corin-induced SE splicing events in ATRT and breast cancer. Enrichment analysis was performed using the hypergeometric test with multiple test correction by the Benjamini-Hochberg method.

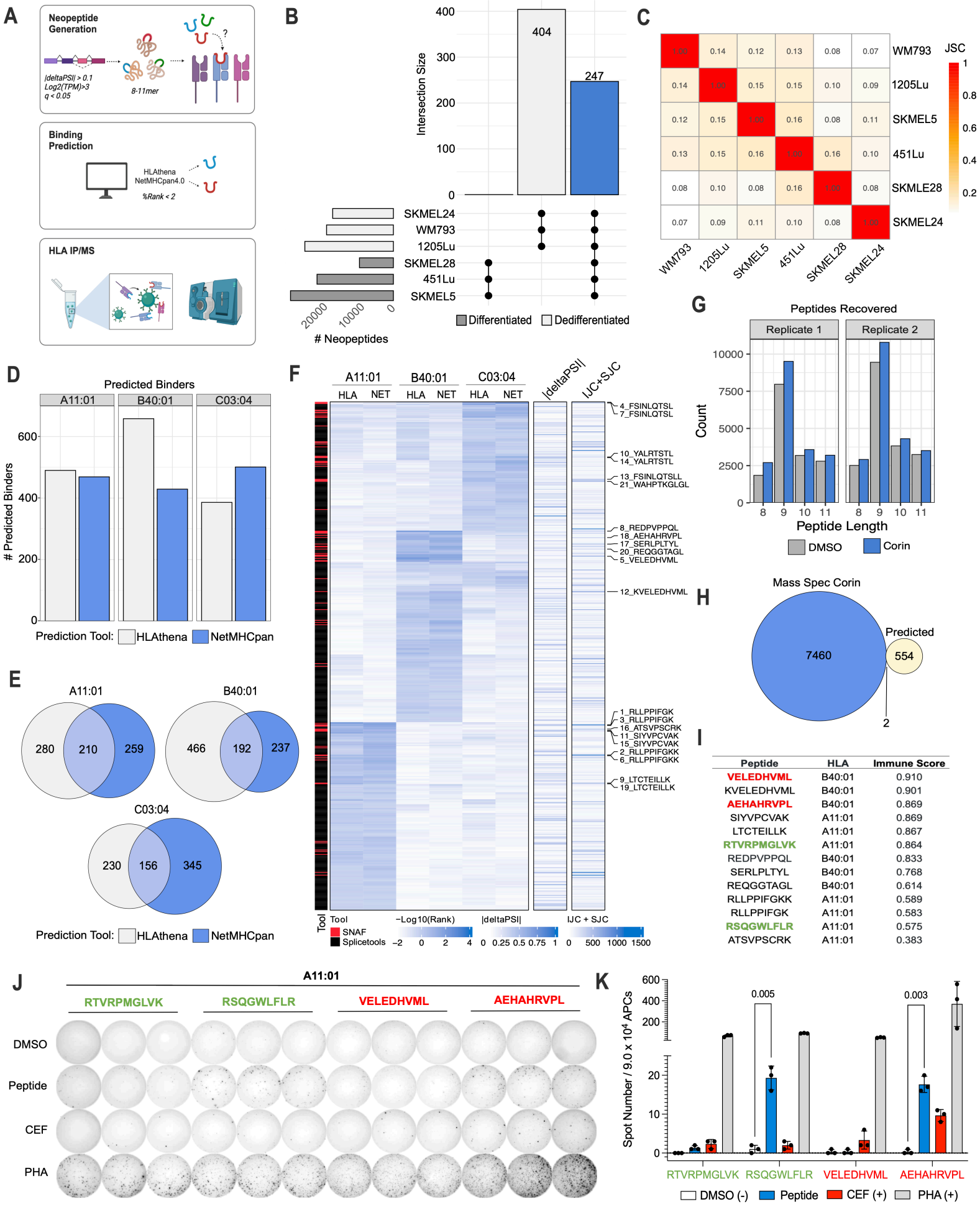
A
Neopeptide Generation
|deltaPSI| > 0.1
Log2(TPM)>3
q < 0.05
8-11mer
Binding Prediction
HLAthena
NetMHCpan4.0
%Rank < 2
HLA IP/MS
B
Intersection Size
404
247
SKMEL24
WM793
1205Lu
SKMEL28
451Lu
SKMEL5
# Neopeptides
Differentiated
Dedifferentiated
C
JSC
WM793
1205Lu
SKMEL5
451Lu
SKMEL28
SKMEL24
D
Predicted Binders
A11:01
B40:01
C03:04
# Predicted Binders
Prediction Tool: HLAthena NetMHCpan
E
A11:01
280
210
259
B40:01
466
192
237
C03:04
230
156
345
Prediction Tool: HLAthena NetMHCpan
F
A11:01
B40:01
C03:04
HLA
NET
|deltaPSI|
IJC+SJC
4_FSINLQTSL
7_FSINLQTSL
10_YALRTSTL
14_YALRTSTL
13_FSINLQTSLL
21_WAHPTKGLGL
8_REDPVPPQL
18_AEHAHRVPL
17_SERLPLTYL
20_REQGGTAGL
5_VELEDHVML
12_KVELEDHVML
1_RLLPPIFGK
3_RLLPPIFGK
16_ATSVPSCRK
11_SIYVPCVAK
15_SIYVPCVAK
2_RLLPPIFGKK
6_RLLPPIFGKK
9_LTCTEILLK
19_LTCTEILLK
Tool
SNAF
Splicetools
−Log10(Rank)
|deltaPSI|
IJC + SJC
G
Peptides Recovered
Replicate 1
Replicate 2
Count
Peptide Length
DMSO
Corin
H
Mass Spec Corin
7460
Predicted
554
2
I
Peptide | HLA | Immune Score
VELEDHVML | B40:01 | 0.910
KVELEDHVML | B40:01 | 0.901
AEHAHRVPL | B40:01 | 0.869
SIYVPCVAK | A11:01 | 0.869
LTCTEILLK | A11:01 | 0.867
RTVRPMGLVK | A11:01 | 0.864
REDPVPPQL | B40:01 | 0.833
SERLPLTYL | B40:01 | 0.768
REQGGTAGL | B40:01 | 0.614
RLLPPIFGKK | A11:01 | 0.589
RLLPPIFGK | A11:01 | 0.583
RSQGWLFLR | A11:01 | 0.575
ATSVPSCRK | A11:01 | 0.383
J
A11:01
RTVRPMGLVK
RSQGWLFLR
VELEDHVML
AEHAHRVPL
DMSO
Peptide
CEF
PHA
K
Spot Number / 9.0 x 10^4 APCs
0.005
0.003
RTVRPMGLVK
RSQGWLFLR
VELEDHVML
AEHAHRVPL
DMSO (-)
Peptide
CEF (+)
PHA (+)

**Figure 7. Corin-induced splicing produces neoantigens that bind human MHC and are immunogenic. (A)** Overview of neopeptide discovery and MHC binding predictions **(B)** UpSet plot of neopeptides (8-11mers) produced with corin treatment of melanoma cells that are exclusive to the differentiated phenotype, dedifferentiated phenotype, or shared by all cell lines (blue). **(C)** Jaccard similarity index comparing corin-induced neopeptide production across all melanoma cell lines. **(D)** Number of corin-induced neopeptides predicted to bind to SKMEL5 HLAs based on two prediction tools: HLAthena and NetMHCPan4.1 (%Rank < 2). **(E)** Overlap of SKMEL5 corin-induced neopeptide HLA binders for each allele predicted by both tools. **(F)** Heatmap showing binding scores, PSI values, and junction counts of predicted SKMEL5 corin-induced neopeptides identified by SNAF and Splicetools. The top 15 unique candidates are labeled. **(G)** Histogram plots of peptides recovered from MHC-IP/MS in SKMEL5 DMSO and corin-treated (72h, 1μM) samples for each replicate (n=2). **(H)** Identification of SKMEL5 corin-induced neopeptides recovered by MHC IP-MS. Corin-exclusive peptides are those identified from the IP-MS that appear in at least one corin replicate but neither DMSO replicate. Predicted peptides are those identified by binding scores in (F). **(I)** Immunogenicity score predictions for neopeptide candidates. Green peptides are those identified from IP-MS and red peptides are additional candidates selected for immunogenicity validation assays based on immunogenic prediction and scores from (F). **(J)** Ex vivo IFNγ ELISpot assay for each candidate neopeptide tested with CEF and PHA positive controls. HLA-matched PBMCs were pre-stimulated with synthesized peptides (10μg/ml) for 14 days in IL2/IL7 media. APCs were isolated from CD4 and CD8 depleted PBMCs, loaded with peptides (10μg/ml), and seeded at a ratio of 3:1 with the pre-stimulated T cells in a 96 well ELISpot plate and analysed for IFNγ + T cells. **(K)** Quantification of ex vivo IFNγ ELISpot assay illustrated in (J). Statistical analysis was performed using multiple two-tailed unpaired t-tests. Error bars represent the standard deviation (SD).

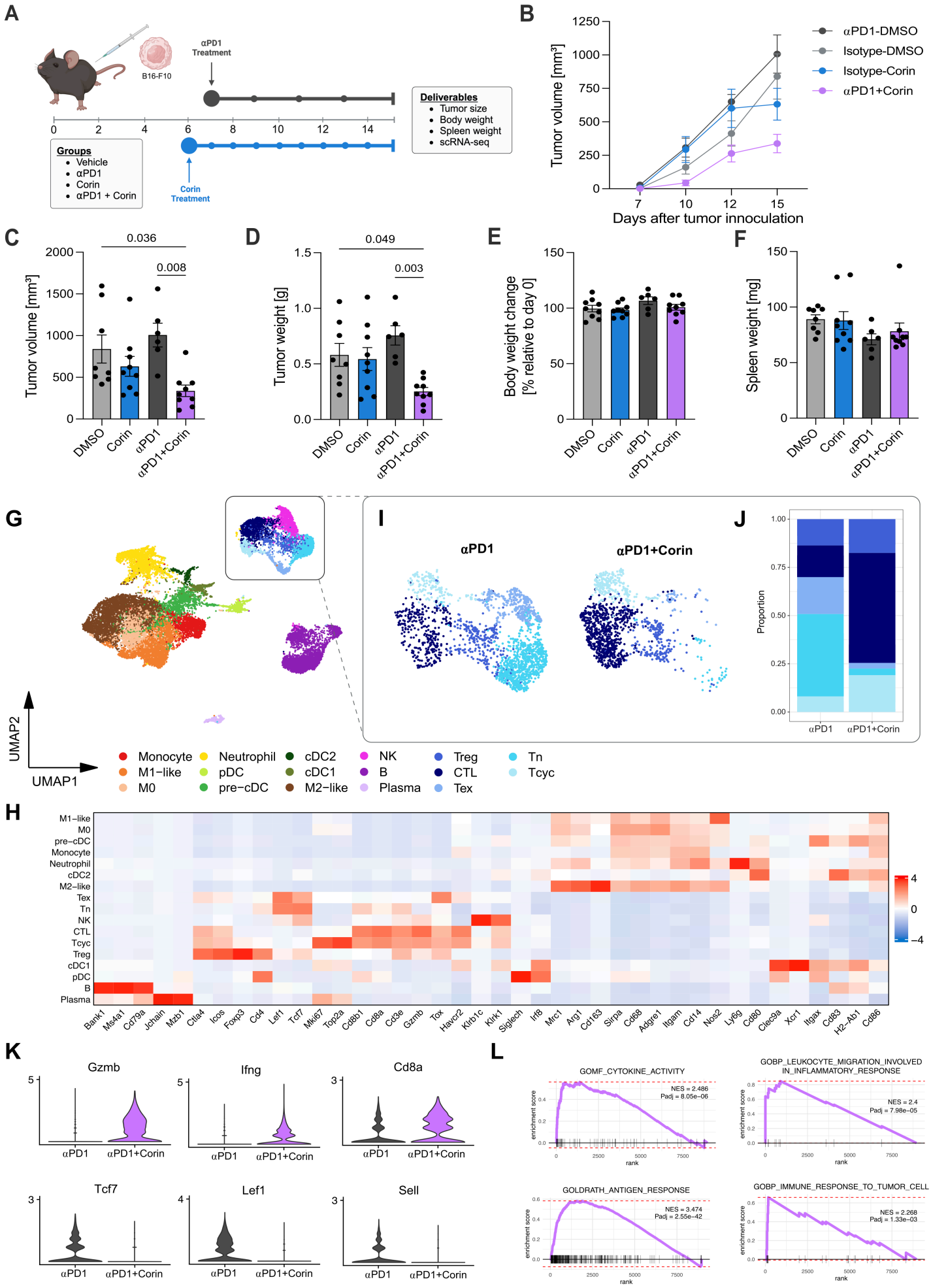
A
B16-F10
αPD1 Treatment
Corin Treatment
Groups
Vehicle
αPD1
Corin
αPD1 + Corin
Deliverables
Tumor size
Body weight
Spleen weight
scRNA-seq
B
Tumor volume [mm³]
Days after tumor innoculation
αPD1-DMSO
Isotype-DMSO
Isotype-Corin
αPD1+Corin
C
Tumor volume [mm³]
0.036
0.008
D
Tumor weight [g]
0.049
0.003
E
Body weight change [% relative to day 0]
F
Spleen weight [mg]
DMSO
Corin
αPD1
αPD1+Corin
G
UMAP2
UMAP1
Monocyte
M1−like
M0
Neutrophil
pDC
pre−cDC
cDC2
cDC1
M2−like
NK
B
Plasma
Treg
CTL
Tex
Tn
Tcyc
I
αPD1
αPD1+Corin
J
Proportion
H
M1−like
M0
pre−cDC
Monocyte
Neutrophil
cDC2
M2−like
Tex
Tn
NK
CTL
Tcyc
Treg
cDC1
pDC
B
Plasma
Bank1 Ms4a1 Cd79a Jchain Mzb1 Ctla4 Icos Foxp3 Cd4 Lef1 Tcf7 Mki67 Top2a Cd8b1 Cd8a Cd3e Gzmb Tox Havcr2 Klrb1c Klrk1 Siglech Irf8 Mrc1 Arg1 Cd163 Sirpa Cd68 Adgre1 Itgam Cd14 Nos2 Ly6g Cd80 Clec9a Xcr1 Itgax Cd83 H2−Ab1 Cd86
K
Gzmb
Ifng
Cd8a
Tcf7
Lef1
Sell
αPD1
αPD1+Corin
L
GOMF_CYTOKINE_ACTIVITY
NES = 2.486
Padj = 8.05e−06
GOBP_LEUKOCYTE_MIGRATION_INVOLVED IN_INFLAMMATORY_RESPONSE
NES = 2.4
Padj = 7.98e−05
GOLDRATH_ANTIGEN_RESPONSE
NES = 3.474
Padj = 2.55e−42
GOBP_IMMUNE_RESPONSE_TO_TUMOR_CELL
NES = 2.268
Padj = 1.33e−03
enrichment score
rank

**Figure 8. Corin sensitizes immune cold tumors to immunotherapy and promotes expansion of tumor infiltrating cytotoxic T cells. (A)** Schematic for corin + immunotherapy combination treatment in a melanoma xenograft mouse model. 6-10 week-old female C57BL/6 mice were inoculated with $2.5x10^5$ B16-F10 cells. Mice were treated with 200 µg/mouse of corin or 200 µl vehicle control (5% DMSO/PBS) by daily intraperitoneal injection starting from day 6 after tumor initiation. For anti-PD1 treatment, mice were treated with 150 µg/mice anti-PD1 or isotype control antibody 3 times/week starting from day 7 post-tumor grafting. 10 mice were included in each treatment group. Tumors were measured 3 times/week and tumor volume, tumor weight, body weight change, spleen weight were measured. **(B)** Line plot and **(C)** quantification of tumor volumes from day 7 to day 15 comparing DMSO, α-PD1, corin, and α-PD1 + corin treatment. **(D)** Histogram of tumor volumes depicted in (B). **(E)** Histogram of body weight change relative to day 0 in animals treated with DMSO, α-PD1, corin, and α-PD1 + corin. **(F)** Histogram of spleen weights in animals treated with DMSO, α-PD1, corin, and α-PD1 + corin. Statistical analyses for panels (C-F) were performed using an ordinary one-way ANOVA with Holm-Sidak's correction for multiple comparisons. Error bars represent the standard deviation (SD). **(G)** scRNA-seq UMAP of the immune population (CD45+) isolated from B16-F10 melanomas. **(H)** Heatmap of the marker genes used to define immune subpopulations in (G). **(I)** Subset UMAP of the T cell compartment comparing α-PD1 treatment to the combination of α-PD1 + corin. **(J)** Stacked barplot of the T cell compartments in (I) **(K)** Violin plots of significant DEGs (Log2FC > |1|, p.adj < 0.05) in T cell populations isolated from α-PD1 versus α-PD1 + corin-treated B16-F10 melanomas. **(L)** GSEA plots for T cell populations isolated from α-PD1 versus α-PD1 + corin-treated B16-F10 melanomas showing enrichment for cytokine activity, leukocyte migration in inflammation, antigen response and immune response in the α-PD1 + corin-treated tumors.

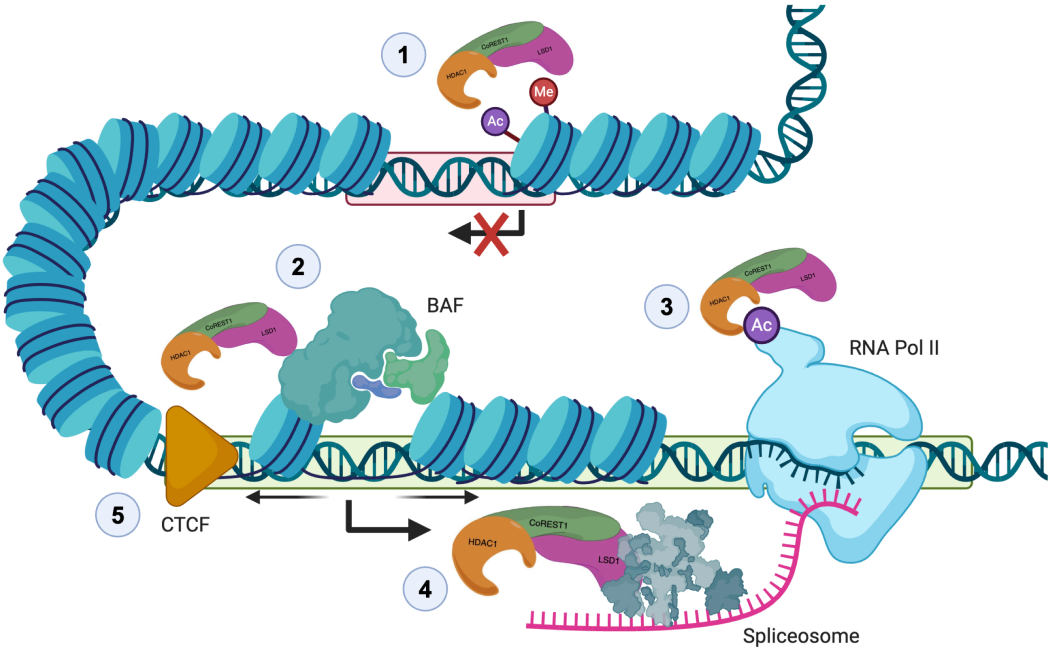
1
CoREST1
LSD1
HDAC1
Me
Ac
2
BAF
3
RNA Pol II
5
CTCF
4
Spliceosome

**Figure 9 Proposed model for multilayered CoREST complex functions in epigenetic regulation, transcription, splicing, and chromatin architecture.** Illustration of CoREST functions and layers of epigenetic crosstalk which ensure transcript fidelity at transcriptionally repressed (red box) and active (green box) regions. (1) Canonical function of CoREST in epigenetic repression through removal of active marks from histone tails. (2) CoREST interactions with the nucleosome-remodeling complex, BAF, promote open chromatin structure at transcriptionally active sites. (3) CoREST deacetylation of Pol II CTD impacts transcriptional kinetics (4) CoREST interactions with the pre-mRNA splicing machinery impacts RNA splicing, alternative transcript expresson and the development of neoantigens. (5) CoREST interactions with CTCF and regulation of higher-order chromatin structure.

**Supplementary Figure 1. Data processing pipeline for cryo-EM analysis and structural superimpositions. (A)** Data processing pipeline to determine the cryo-EM structure of U2AF2 bound to the LSD1+RCOR1 complex. **(B)** Fourier Shell correlation plot showing a global resolution of 5.14 Å. **(C)** Local resolution estimation showing a cryo-EM map resolution range from 5.0 Å to 7.0 Å. **(D)** Superimposition of LSD1+RCOR1 over the EM density showing an excellent fit. **(E)** Superimposition of the RRM2 domain of U2AF2 over the U2AF2 EM density showing a good fit. **(F)** Superimposition of the UHM domain of U2AF2 over the U2AF2 EM density showing a poor fit. **(G)** SDS-PAGE and Coomassie staining of purified and fluorophore (Cy5)-labeled U2AF2 fragments. **(H)** Capillary scan data demonstrating successful fluorophore labeling (Right). This data was collected before and after the MST measurement to assess the robustness of fluorophore-labeled U2AF2 fragments binding with truncated LC. Sixteen capillaries were scanned and analyzed, revealing symmetrical peaks with appropriate intensities. **(I)** MST traces measuring the binding affinity between the U2AF2 fragment and truncated LC. A 20-s time window, highlighted in red, has been selected due to its favorable signal-to-noise ratio. The time prior to the IR laser activation is marked in blue. **(J)** Dose-response curve of the MST assay measuring the binding affinity between the U2AF2 fragment and truncated LC. Three replicates were applied.

**Supplementary Figure 2. CoREST inhibition does not impact splicing factor transcript steady state. (A)** Diagram of KEGG Spliceosome pathway with genes downregulated by corin treatment highlighted in pink. **(B)** Western blot biological replicates used in the quantification of Fig. 3E. **(C)** Gene set enrichment analysis for the KEGG Spliceosome gene set using expression data derived from PRO-seq ($q < 0.05$). **(D)** Heatmap comparing PRO-seq to RNA-seq Log2FC values across the significant downregulated splicing factors.

**Supplementary Figure 3. AltAnalyze results of differential RNA splicing in melanoma cell lines.** Summary of significant RNA splicing changes across six melanoma cell lines treated with corin (deltaPSI $\geq$ |0.1|, $p < 0.05$) in duplicate detected by AltAnalyze.

**Supplementary Figure 4. CoREST inhibition impacts RNA splicing factor intron retention and selectively skips short exons. (A)** Exon and proximal intron length bias between differentially included and excluded exons. Statistical analysis was performed using ANOVA to compare lengths across treatment groups, grouped by type of splicing event. P-values were adjusted for multiple comparisons using the Holm-Sidak's correction. **(B)** Exon and proximal GC bias between differentially included and excluded exons. Statistical analysis was performed using ANOVA to compare GC content across treatment groups, grouped by type of splicing event. P-values were adjusted for multiple comparisons using the Holm-Sidak's correction. **(C)** Percent Spliced In (PSI) distribution across 6 melanoma cells lines for significant Intron Retention (RI) events detected by AltAnalyze (deltaPSI $\geq$ |0.1|, $p < 0.05$). Statistical comparisons were performed using a two-sample t-test to assess differences in PSI value between treatment groups within each cell line. **(D)** Pathway analysis for significant RI events across the 6 melanoma cell lines ($p < 0.05$). Enrichment analysis was performed using the hypergeometric test with multiple test correction by the Benjamini-Hochberg method.

**Supplementary Figure 5. RNA-SPRINT analysis of RBP activity correlated with corin-induced expression changes. (A)** Rank plot of Spearman's rank correlation between RBP activity and expression with corin treatment. Red points denote RBPs with a correlation value > 0.5. **(B)** RBP activity scores for each candidate RBP determined in (A) across all 6 melanoma cell lines. **(C)** Individual correlation plots for each candidate RBP. **(D)** rMAPS2 coverage plots for U2AF2 binding scores in significantly included (blue) and excluded (red) exons in SKMEL5 cells

treated with corin compared to a randomized background list of exons (black). Motif scores are represented by solid lines and p-values are represented by dashed lines. The window is centered at the expons of interest (green box).

**Supplementary Figure 6. Validation of corin-induced RNA splicing changes. (A)** Sashimi plots of MYO1B, TJP1, and FN1 splicing based on RNA-seq data. **(B)** TJP1 exon 20 RT-PCR gel comparing DMSO, LSD1i, HDACi, LSD1i + HDACi, and corin's impact on exon inclusion. Statistical analysis of biological replicates (n=3) was performed using an unpaired, two-tailed t-test. Error bars represent the standard deviation (SD). **(C)** RT-PCR gel biological replicates used for quantification in Fig. 5A and S5B.

**Supplementary Figure 7. U2AF2-binding does not impact LSD1's demethylase or LHC's deacetylase activity. (A)** The effect of U2AF2 on LSD1 demethylase activity was evaluated using a horse radish peroxidase (HRP)-coupled peptide demethylase assay. GST-LSD1$_{171-852}$ and H3K4me2 peptide (aa 1-21) were used as the enzyme and the substrate, respectively, in the assay with and without U2AF2$_{241-471}$. $H_2O_2$ generated from the demethylation reaction was coupled with HRP to catalyze a chromogenic reaction between 4-aminoantipyrine and 3, 5-dichloro-2-hydroxybenzenesulfonate (DHBS) that allows detection at 515 nm Initial rates of product formation (V/[E], $min^{-1}$) were calculated from three technical replicates, based on measurements taken between 2–4 minutes of the reaction. Data were analyzed using Graphpad Prism 10 with an unpaired, two-tailed Student's t-test, testing the null hypothesis that LSD1 activity does not differ with and without U2AF2$_{241-471}$. **(B)** Representative western-blot images describing deacetylation of H3K9ac nucleosome by the LHC complex with or without U2AF2. **(C)** Enzymatic activity (V/[E]) of the LHC complex toward the H3K9ac site on nucleosomes in the absence and

presence of U2AF2. Conditions: [Nucleosome] = 100 nM; [LHC] = 40 nM; [U2AF2] = 10 μM; All values denote mean ± s.e.m; n = 4; Student's *t*-test.

**Supplementary Figure 8. Corin promotes promoter pause release without impacting transcriptional kinetics at splice sites**. **(A)** PRO-seq coverage metagene plot centered at TSS's under DMSO or corin conditions. **(B)** Pausing index calculated between treatments. Statisical analysis performed using a two-sided two-sample t-test. **(C)** PRO-seq coverage metagene plots at 3'SS and 5'SS for significantly included and excluded skipped exon events (deltaPSI $\geq$ |0.1|, q < 0.05).

**Supplementary Figure 9. CoREST-regulated RNA splicing factors are frequently overexpressed across cancers.** Oncoprint plot depicting the frequency of altered mRNA expression alteration in CoREST complex-regulated RNA splicing factors between cancer and matched normal tissue from cBioPortal stratified by cancer type. Pink bars indicate the frequency of overexpression events and blue bars indicate the frequency of downregulation events.

**Supplementary Figure 10. CoREST-regulated splicing is concordant across cancers. (A)** Summary of significant RNA splicing changes across ATRT and breast cancer cell lines treated with corin (deltaPSI $\geq$ |0.1|, p < 0.05) in duplicate detected by AltAnalyze. **(B)** Heatmap showing concordance between cell lines based on common SE splicing events. **(C)** Heatmap showing concordance between cell lines based on common AP splicing events. **(D)** UpSert plot comparing the total number of phenotype specific AP events across melanoma cell lines **(E)** GO dotplot of significant pathways impacted by differential AP inclusion across melanoma cell lines.

**Supplementary Figure 11. Additional immunological analyses to validate neoantigen immunogenicity and corin's impact on the tumor microenvironment.** ELISpot images and quantification for HLA B40:01 **(A)** and HLA C03:04 **(B)**. Statistical analysis was performed using multiple two-tailed unpaired t-tests. Error bars represent the standard deviation (SD). No peptides reached statistical significance. **(C)** scRNA-seq UMAP comparing the immune populations between anti-PD1 and anti-PD1+corin treatment. **(D)** Proportion analysis comparing changes in the immune populations between treatments. **(E)** Barplots and statistical analysis comparing changes in T cell proportions (*p.adj < 0.05, **p.adj < 0.01, ***p.adj < 0.001). **(F)** Volcano plot of differential gene expression in the T cell subset. (G) Representative immunofluorescent images of anti-PD1 and anti-PD1+corin treated B16-F10 melanomas stained for CD3+ and CD8+ T cells.

**Supplementary Table 1. Results from the IP-MS using the LSD1 and RCOR1 pulldowns comparing IgG to DMSO.** Log2(Fold change) and -Log2(p) values were calculated by comparing signal to IgG control.

**Supplementary Table 2. Results from the IP-MS using the LSD1 and RCOR1 pulldowns comparing corin to DMSO.** Log2(Fold change) and -Log2(p) values calculated by comparing DMSO signal to corin signal (24h, 2.5uM).

**Supplementary Table 3. Significant differential splicing events for melanoma cell lines.** Differential events are defined by $q < 0.05$, $\text{deltaPSI} \geq |0.1|$.

**Supplementary Table 4. Pausing Index values calculated from PRO-seq data.** PI values from DMSO and corin treated samples.

**Supplementary Table 5. CoREST-regulated splicing factors.** List of splicing factors significantly downregulated in all melanoma, ATRT, and breast cancer cell lines.

**Supplementary Table 6. Significant differential splicing events for ATRT and breast cancer cell lines.** Differential events are defined by q < 0.05, deltaPSI ≥ |0.1|.

**Supplementary Table 7. Summary of significant predicted neopeptides.** Neopeptide candidates were selected based on the product of the -$Log10$(%Rank), junction count, and |deltaPSI| value (q < 0.05, deltaPSI ≥ |0.1|, $Log2$(TPM) ≥ 3, IJC + SJC ≥ 20, % Rank $\leq$ 2).

**Supplementary Table 8. Peptides identified from MHCI IP-MS.** Peptides were identified using MSFlagger and MaxQuant (FDR < 0.05).

**Supplementary Table 9. List of antibodies.**

**Supplementary Table 10. List of primers.**